School of Chemistry

Fabrication and evaluation of p-type Schottky diamond diodes for beta voltaic batteries

Jacob Fox

This thesis is submitted in partial fulfilment of the requirements for the Honours Degree of BSc at the University of Bristol

Supervisor: Professor Neil A. Fox

2nd Assessor: Professor Paul W. May

Section: Physical and Theoretical Chemistry

Statement of factors that limited project progression

The back reactor was shut down for maintenance and regeneration over the Christmas holidays with an expected completion date near the start of the second semester. Difficulties with parts shipping and reactor assembly meant the back reactor was unfortunately not ready for use until after the conclusion of this project meaning a notable number of growth runs had to be completed on the front microwave reactor and the hot filament reactor.

This led to much longer lead times in the development of the chips as the front reactor was then occupied more frequently and growth runs were more difficult to schedule as a fair balance had to be struck by the increased volume of users.

In addition, the front reactor suffered numerous faults during its use in the second semester. This was the result of other work being conducted in the lab that led to large pressure fluctuations within the chamber. These pressure fluctuations caused unsafe movement of the plasma in the chamber, in one case leading to the destruction of two samples and in another causing significant damage. To quantify the damage done by these two malfunctions alone, approximately 12 hours of work was undone in moments.

Abstract

High-power, high-efficiency diamond-based diodes are generally considered the cutting edge of current semiconductor technology, especially in the areas of power electronics and betavoltaics. This project aimed to synthesise and characterise diamond Schottky diodes using microwave plasma-assisted chemical vapor deposition for betavoltaic application.

The project also focuses on the development and optimisation of a diode structure based upon a silicon-supported diamond membrane produced by a multi-step etching procedure after the heteroepitaxial growth of diamond on a silicon wafer.

Two freestanding diamond Schottky diodes were developed via the growth of an intrinsic polycrystalline diamond layer on an Element Six boron-doped diamond sample and aluminium metal Schottky and ohmic contacts were applied by vacuum evaporation. The synthesised diodes were evaluated by conducting current-voltage measurements using a Keithley 2401 source meter. One of the diodes was subjected electron irradiation while applying a voltage bias of -200V using a Kimble Physics flood gun to simulate the diode being exposed to weak beta radiation characteristic of tritium and nickel-63 radioactive decay. Another sample was tested directly with low activity beta radiation from a potassium-40 source. Both samples exhibited measurable responses to their environment providing exciting, early-stage outlooks on future applications of diamond voltaics.

Acknowledgements

Firstly, I would like to thank Professor Neil Fox, who as my supervisor provided consistent support in this project as well as sparking my interest in the sector of physical material chemistry and came up with thought provoking conversations into his area of scientific interest.

I must also thank Ms Catherine Monk not only for training me on the microwave reactor and Raman spectrometer but also for being a constant source of support when I was facing difficulties in the project.

I would also like to acknowledge Dr Ramiz Zulkharnay for his continued support throughout the project, answering many of my questions which kept me constantly engaged and curious to learn more during the process.

I am also grateful for the support of Mr Liam Cullingford throughout the project. His continued work to build the electron beam was important for my results and his willingness to answer my questions did not go unappreciated.

I couldn’t go without mentioning my peers throughout this project, namely Axel Persson, Benjamin Harding and James Swarbrigg – perhaps less creatively named the ‘Diamond Boys’. It is hard to believe people I only met 6 months ago now seem like lifelong friends, their constant support and motivation throughout the project made the lab a thoroughly enjoyable place to work and I wish them well as they seek out postgraduate study.

I would finally like to thank my family and partner who have provided unending support throughout this challenging phase in my academic career.

Contents

1. Introduction

1.1 Diamond and nuclear power context

For centuries, diamond's sole purpose has been a status symbol for the wealthy. Only recently has it been utilised for purposes outside of jewellery, with common uses in hardware for tools and computing. However, it is the advances in lab grown diamond synthesis which could be pivotal over the next century for energy storage and production, a potential an answer to humanities growing green energy crisis. With the rising concern of global warming, many scientific critics point towards nuclear energy as an ideal solution, with immense power outputs and low greenhouse gas emissions[1]. Global utilisation of nuclear energy opens the door for a new set of problems; nuclear waste containment and disposal. This is where synthetic diamond chemistry could prove a useful commodity by storing and generating power from low level nuclear waste such as nickel-63, a compound which otherwise would have no use and be disposed of deep into geological sites[2]. Advances in nuclear technology such as betavoltaic batteries has indisputably been slowed as a result of the societal fear of nuclear energy caused by nuclear weapon proliferation and disasters such as Chernobyl & Fukushima[3, 4].

1.2 Carbon allotropes

Carbon exists in many allotropes which each offer unique and identifiable characteristics. Diamond, which forms as a giant covalent lattice of sp^3 hybridised carbon, is the most renowned allotrope[5]. The highly covalent sp^3 lattice results in a rigid structure with no free electrons. This gives rise to scarcely rivalled mechanical properties such as a boiling point of 4830 °C and a hardness of 10 on the Mohs scale.

Carbon is more commonly found as its other allotrope, graphite, a less famous but vastly more prevalent sibling of diamond. Graphite consists of sheets of sp^2 hybridised carbon atoms, leaving a pair of delocalised electrons which give rise to conductivity. Graphite's conductivity and chemical inertness make it an ideal electrode material in electrochemical batteries. In the case of a nuclear micro batteries, which rely on a semiconductor rather than a fully conductive material, graphite has limited opportunity for exploitation.

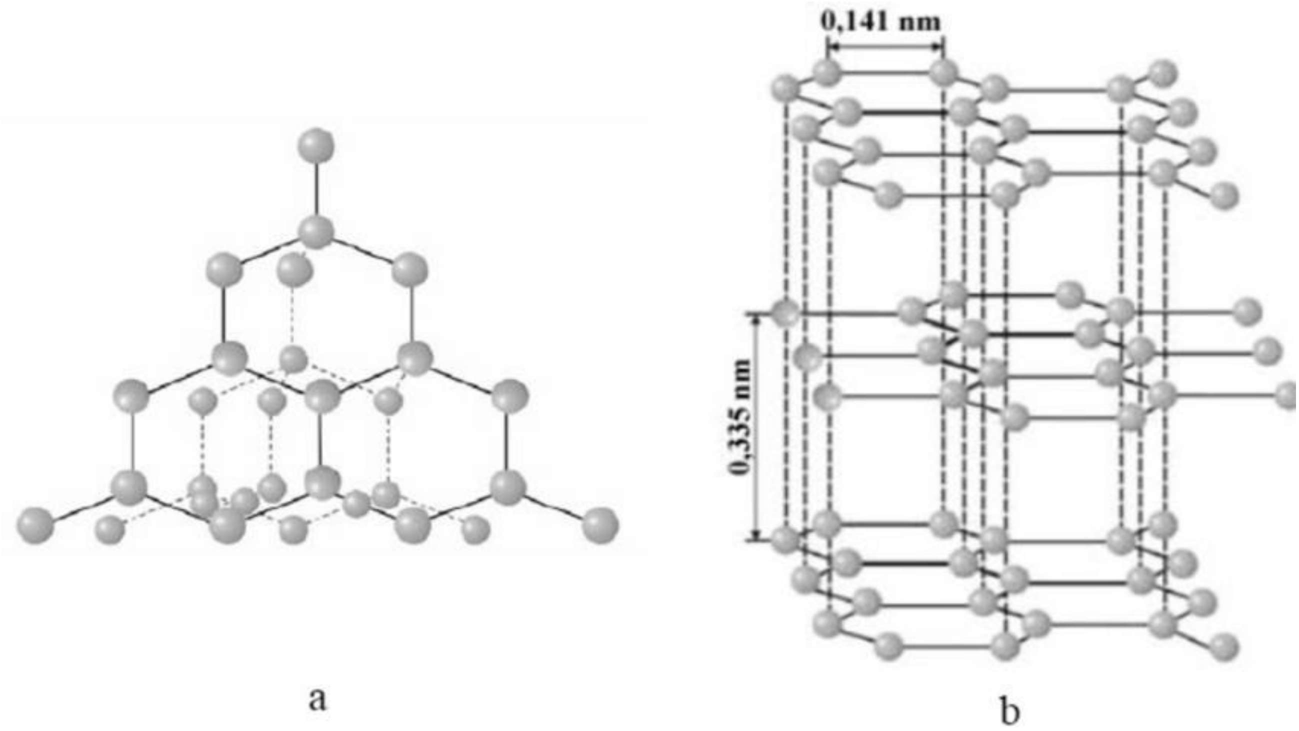

Figure 1 - The crystal lattices of diamond (a) and graphite (b). Sp^3 hybridised carbon in diamond has a bond length of 1.54 Å and the sp^2 hybridised carbon in graphite has an average bond length of 1.418 Å. Diamond has a unit cell dimension of 3.567 Å whereas graphite exhibits unit cell dimensions of 2.46 x 2.46 x 6.71 Å[6]*.*

2. Properties of Diamond

2.1 Diamond structure & polycrystalline diamond

The surface orientation of synthetic diamonds can be defined by the Miller Indices (111, 100 and 110). These numbers are related to the intersection of the plane with the main crystallographic axes and the given identity is significant for understanding surface properties[7].

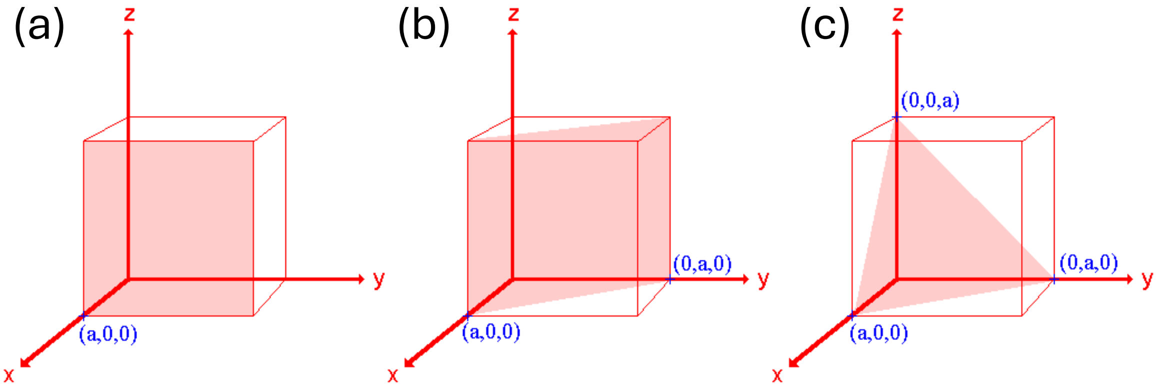

Figure 2 - Diagrams of the 3 major surface morphologies of lab grown diamond. Image (a) depicts the (100) plane while (b) and (c) depict the (110) and (111) planes respectively[7].

Most available chemical vapor deposition (CVD) diamond is grown with a (100) surface and (110) vertices[8]. Studies by Su et al. show that (100) faceted diamond has better properties than (111) diamond such as more consistent electrical properties, and a reflective index closer to that of natural diamond[9].

Polycrystalline diamond grows without order and in multiple surface orientations. This leads to significant grain boundaries which have been shown to contain a higher density of defects which effect electrical transport. At lower temperatures, electrical transmission is dominated by grain boundary defects, however at higher temperatures the crystalline grains contribute to transport – leading to a nonuniform distribution of current flow[10].

2.2 The electrical properties of diamond

Diamond is known for its immense physical properties, often hailed as one of hardest materials in existence ($9x10^{9}$ kg m^{-2}) with a thermal conductivity five times higher than copper (>2000 $Wm^{-1}K^{-1}$ vs 100-500 $Wm^{-1}K^{-1}$)[11-13]. High thermal conductivity is a vital attribute for high power applications and extends device lifespan as degradation is less likely. These physical properties are of great importance but would ultimately prove useless with respect to nuclear micro batteries without other key electrical attributes. The high resistivity ($1x10^{16}$ Ωm), carrier mobility, and electric breakdown field are properties which lend themselves excellently to the use of a semiconductor diode; however some chemical alteration is necessary to introduce free charge carriers[14-16]. A high resistivity is imperative for a betavoltaic diode because it enables their fundamental role as a one-way conductor. Utilising high resistance for rectification purposes in electrical devices allows device charging, as mains AC can be converted to DC power in order to charge a battery. In the case of a betavoltaic cells, this rectification is important for directing charge flow, preventing electron hole recombination, and optimising power extraction in a nuclear micro battery. In addition, carrier mobility is vital for efficient charge collection and prevention of electron hole recombination. If carriers are less mobile in the substrate, they are more likely to recombine before collection at electrodes thus hampering device efficiency. A high electric breakdown field enables device operation at high voltages and allows for the use of thinner active layers.

3. Industry and Applications of Diamond

3.1 Battery Technology

Since their theorisation in the 70's and commercialisation in the 90's Lithium-ion batteries have grown into the market where they now have a majority foothold[17-19]. Their most common uses exist in the rapidly progressing electric vehicle market, as well as in portable electronic devices due to their high levels of adaptability. Lithium-ion cells store and release energy via the movement of electrons between electrodes.

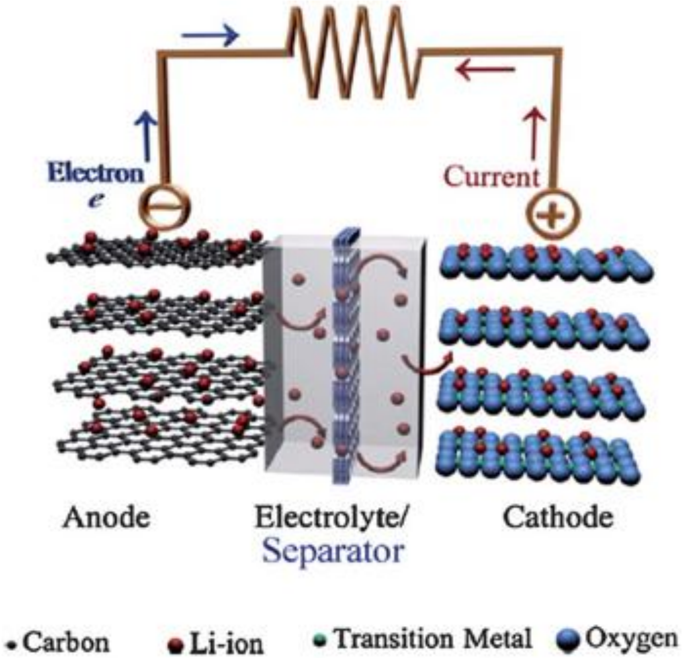

Figure 3 - A lithium-ion cell showing the graphite anode[20].

Despite possessing high power and energy densities compared to other commercial batteries (lead acid and alkaline), Lithium-ion technology falls massively short of betavoltaic batteries when comparing energy density[21]. For this reason, beta voltaic batteries are often used in niche scenarios where a long-lasting energy source is required; for example outer-space or deep-sea electronics where maintenance and accessibility are limited. Unlike Lithium-ion batteries, betavoltaics require a semiconductor. Diamond's high radiative hardness and ability to be doped during CVD growth makes it a growing area of interest in betavoltaic chemistry.

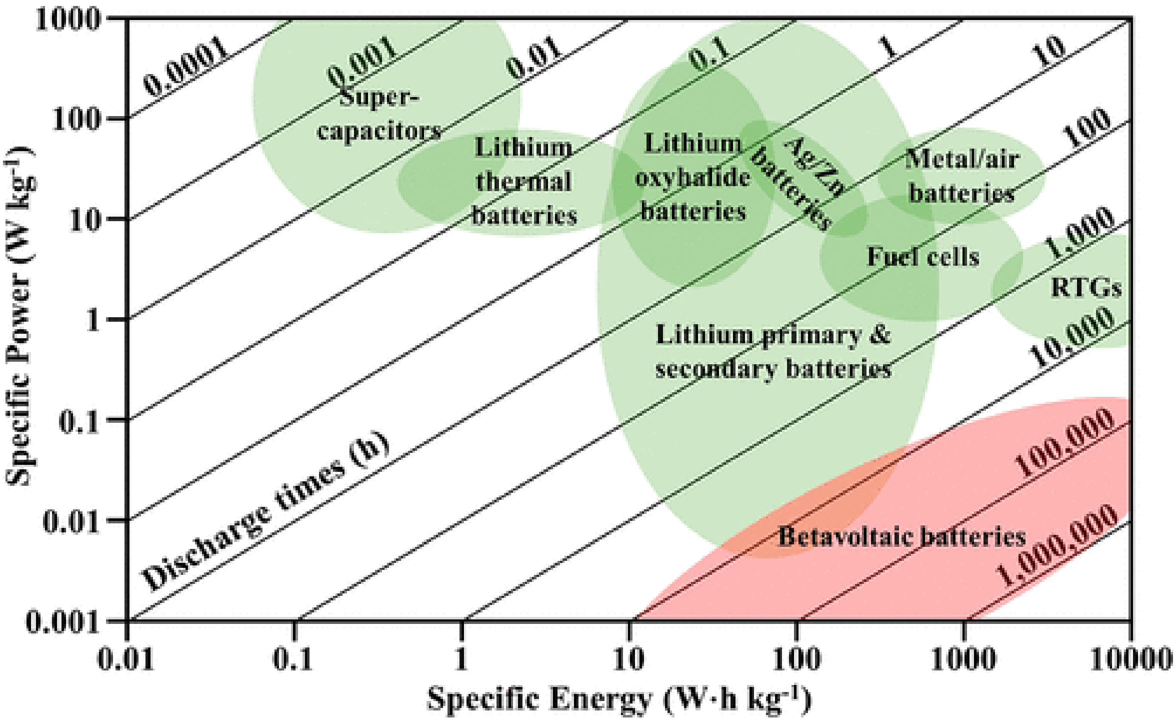

Figure 4 - A graph of energy density vs power density showing betavoltaic batteries with 10-100x the energy density of lithium ion batteries[22].

3.2 Radiovoltaics

Scientists have been aware of the possibility of using radiation in electrical cells since the mid-20th century, even testing their effectiveness as a pacemaker power supply[23]. Ultimately, concerns of radiation exposure and cheaper alternatives caused a decline in interest for the radio isotopic battery industry. Modern advances in diamond synthesis, as well increased efficiency and safety of nuclear-powered batteries, could be the platform for radiovoltaic energy to become far more prominent. As previously stated, diamond has an impressive radiative resistance, also proven by its use as a radiation detector, this means diamond can safely contain a radioisotopic power source[24]. Furthermore, diamond exhibits a wide band gap of ~5.5 eV and extreme thermal conductivity, giving it superior electrical properties compared to its semiconductor competitors[25, 26].

3.3 Diamond and other semiconductor materials

Among most other common semiconductors, diamond is considered an ultrawide bandgap (UWBG) material. Even when compared to other UWBG semiconductors such as gallium nitride (GaN) and silicon carbide (SiC) (~3.4 and 3.26 eV respectively), diamond's band gap is more than 60% larger. This, combined with diamond's high critical electrical field and charge carrier mobility, means that diamond lends itself excellently towards use in high-performance, high-power devices, which may be critical for the progression of scientific technology[27]. Amidst the ever-changing landscape of scientific discovery and computational advancement, one thing remains constant: the necessity for increasingly powerful and capable hardware. Beyond its use in the production of betavoltaic batteries and Schottky diodes, diamond has substantial promise to alter the world of electronics. Quantum and super-computing, high frequency RF devices, extreme environment applications, and high sensitivity sensors are just a few of the potentially benefitting sectors.

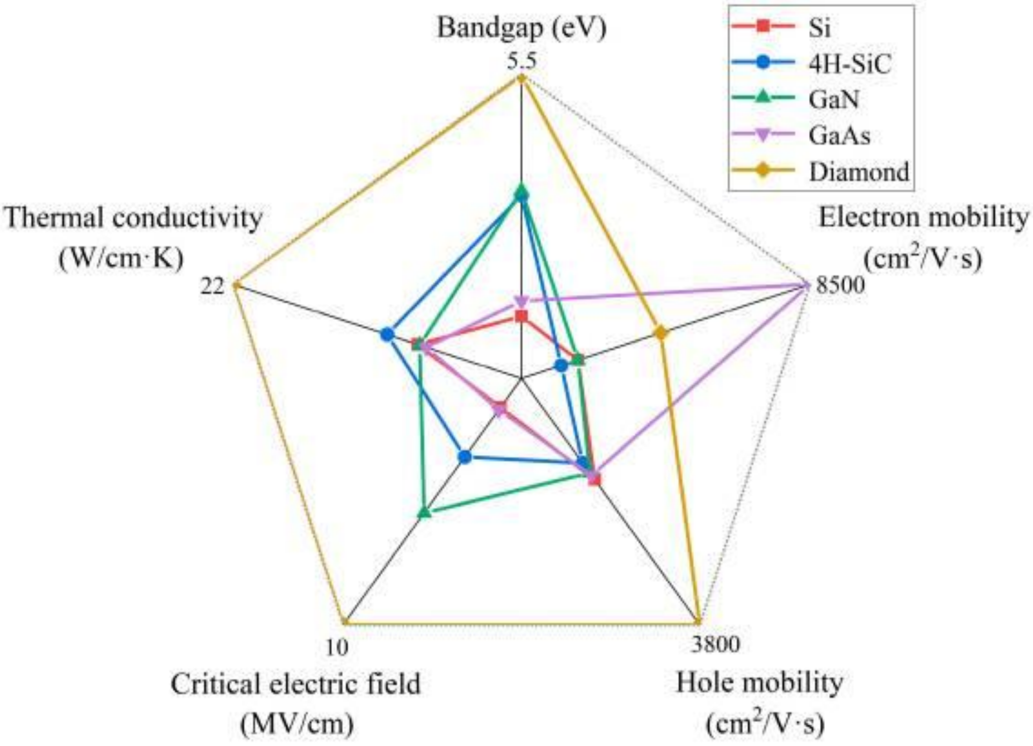

Figure 5 - A radar chart comparing different electrical and physical properties of diamond with other common modern semiconductor technologies[27].

4. Diamond Growth Techniques

4.1 CVD and HPHT – Context and Mechanism

There are two main methods for the production of synthetic diamonds: chemical vapour deposition (CVD), and high pressure high temperature (HPHT).

HPHT, initially achieved by General Electric in 1954, involves the growth of diamond in a high pressure high temperature environment in an attempt to recreate the natural process of diamond formation[28]. To speed up this process, which naturally occurs over billions of years, scientists have developed specific conditions and procedures providing a catalytic effect on diamond growth. The generally accepted process today involves incorporating a high purity carbon source into a molten metal mixture at high temperatures (~1500 °C), and allowing the precipitation of carbon onto cooler diamond seeds held in a mechanical press. This process can take weeks or months to achieve the desired crystal growth[29].

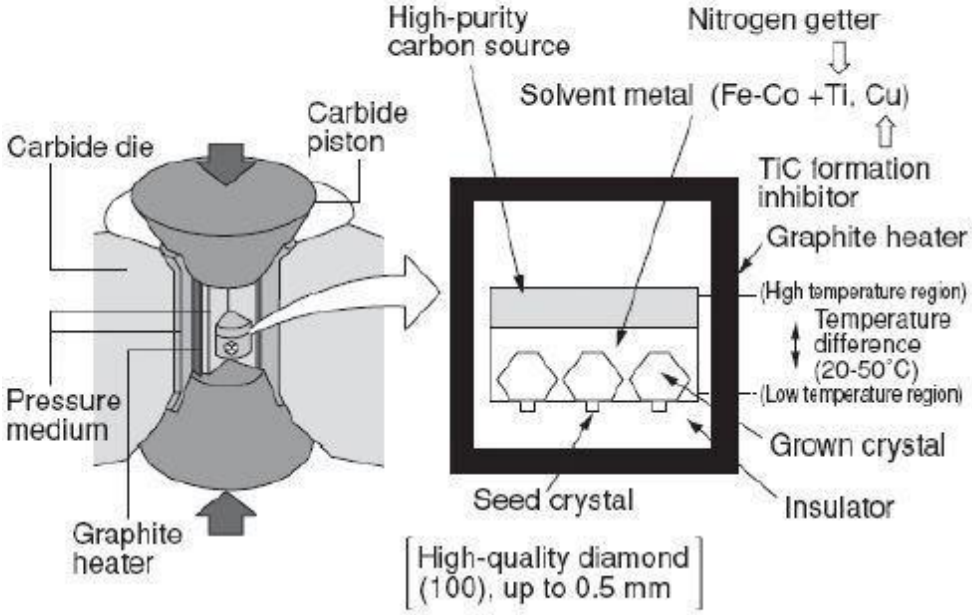

Figure 6 – A detailed schematic of HPHT diamond growth and its mechanism[30].

CVD technology predates HPHT, however increased costs and lack of reporting until a decade later led to a delayed emergence in research and the commercial market. The two major methods include thermal CVD (usually hot filament) and microwave plasma-assisted CVD. Thermal CVD is the oldest and simplest of these methods. It involves the heating of a metal filament to around 700-1000 °C a couple of millimetres above the surface of the solid substrate, and introducing the desired precursor atmosphere at low pressure. The solid substrate is also heated electrically from beneath to temperatures exceeding 2000 °C. The overarching mechanism for CVD is the introduction of gaseous precursors at elevated temperatures to induce activation leading to the eventual deposition of carbon on a solid surface.

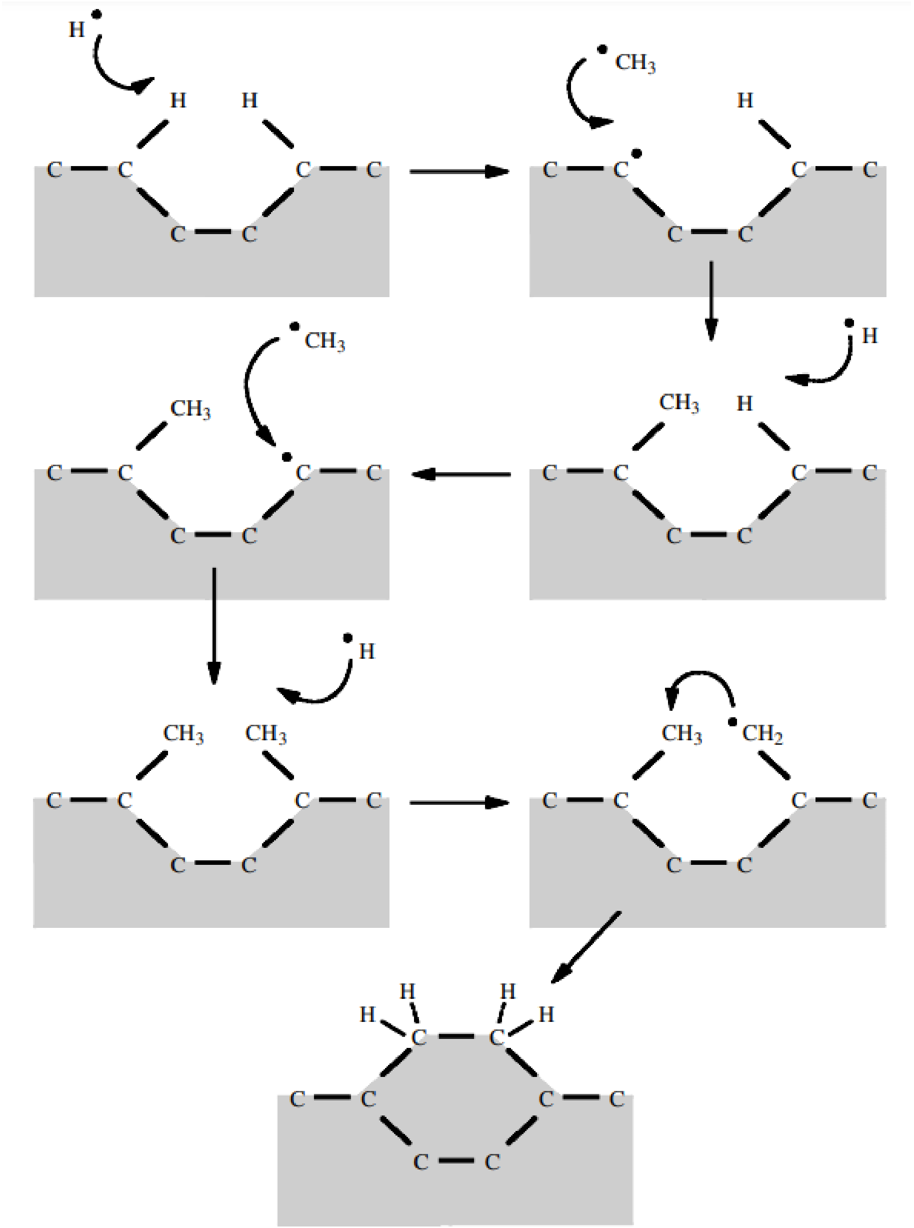

Figure 7 - A simplified mechanism for the growth of diamond at the surface in CVD[31].

Hot filament CVD (HFCVD) is mechanically the simplest form of thin film deposition and can produce high quality films. However, its drawbacks come with the likelihood of contamination and stability of the process, both of which are a result of filament decay. Furthermore, HFCVD has limitations on the gas inputs, as oxygen cannot be present due to oxidation of the tantalum filaments. Despite these limitations, hot filament CVD has notable virtue in that the potential surface area for deposition is much larger than that of microwave plasma-assisted CVD (MPCVD). This is because the machine and filament can be scaled up relatively easily whereas the surface area of deposition in MPCVD is limited to plasma size.

Over the last decade, the most studied and used method of CVD has been MPCVD, a method using high energy microwaves to generate a ball of plasma above a substrate.

The gas phase precursor is introduced into the CVD chamber at low pressure, and the energy from the plasma induces the reaction between gases (usually CH_4 and H_2). The simplest description for the mechanism occurring inside a MPCVD reactor involves high energy microwaves striking the gas inside the chamber, resulting in ionisation and radicalisation of the methane and hydrogen. These activated species then have the ability to interact with the surface of the substrate (e.g. diamond seeds on a manually abraded silicon surface). Hydrogen radicals can strip surface hydrogen termination on the substrate, which provides the possibility for a methyl radical to attack.

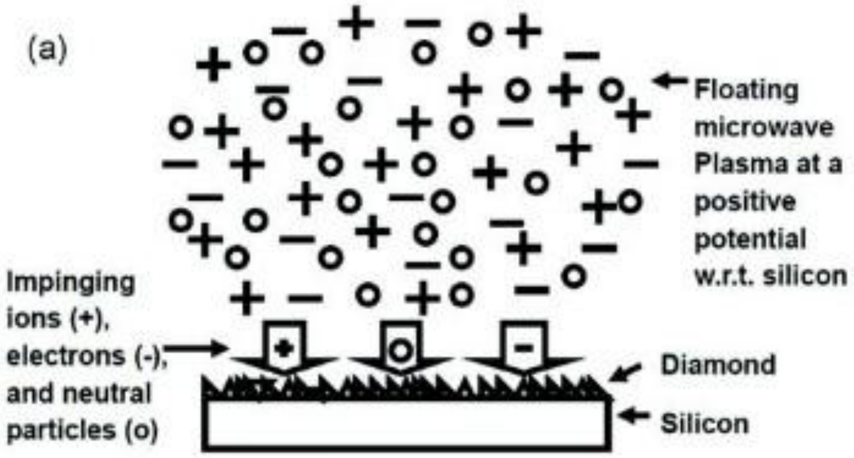

Figure 8 - A simplified image of microwave plasma assisted CVD showing the 'activated' ion cloud above the substrate leading to growth at the surface[32].

This process, however, is incredibly slow and occurs over multiple steps, each of which has a chance of reverting back to its previous state. The fastest growth rate ever recorded was 930 μm/h using DC plasma jet CVD, a newer and more expensive method of CVD[33].

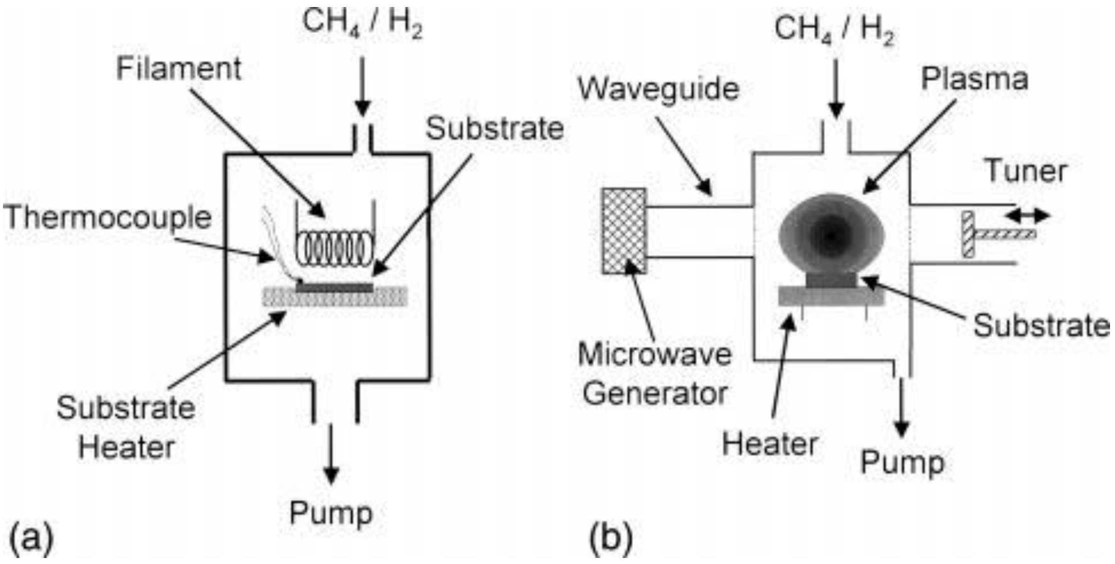

Figure 9 - A schematic of (a) hot filament CVD and (b) microwave plasma-assisted CVD [34].

A key benefit of CVD over HPHT is it can be carried out at lower temperature and pressures, thus reducing the cost of production.

The ability to change the composition of the gas precursor gives rise to varying properties of the deposited material. If the gas phase is made up of entirely hydrogen, carbon, and oxygen, the growth of diamond can be described by the Bachman triangle. This diagram outlines whether product growth will be graphitic, diamond, or if growth will cease altogether.

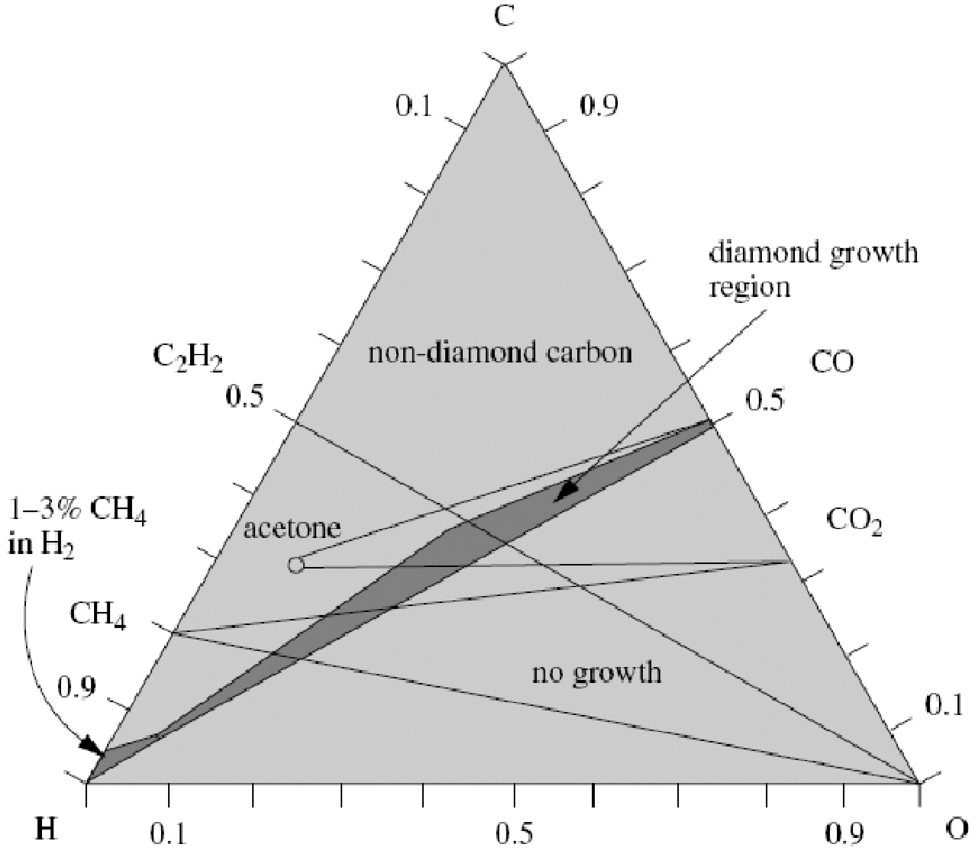

Figure 10 - The Bachman triangle, showcasing the product of CVD dependant on gas precursor mole fractions of carbon, oxygen and hydrogen[35].

Introduction of other compounds, such as nitrogen or diborane, can result in product doping. Doped diamond exhibits different properties from visual to electronic, for example boron doping can change diamond from an insulator to a semiconductor; this specific application is vital for the theory and success of this dissertation. The acceptor energy level produced by boron in boron doped diamond (BDD) has been experimentally demonstrated to sit ~0.37eV above the valence band of diamond. Theoretical models using calculations from first principles have closely predicted the acceptor level as 0.39 eV above the valence band[36].

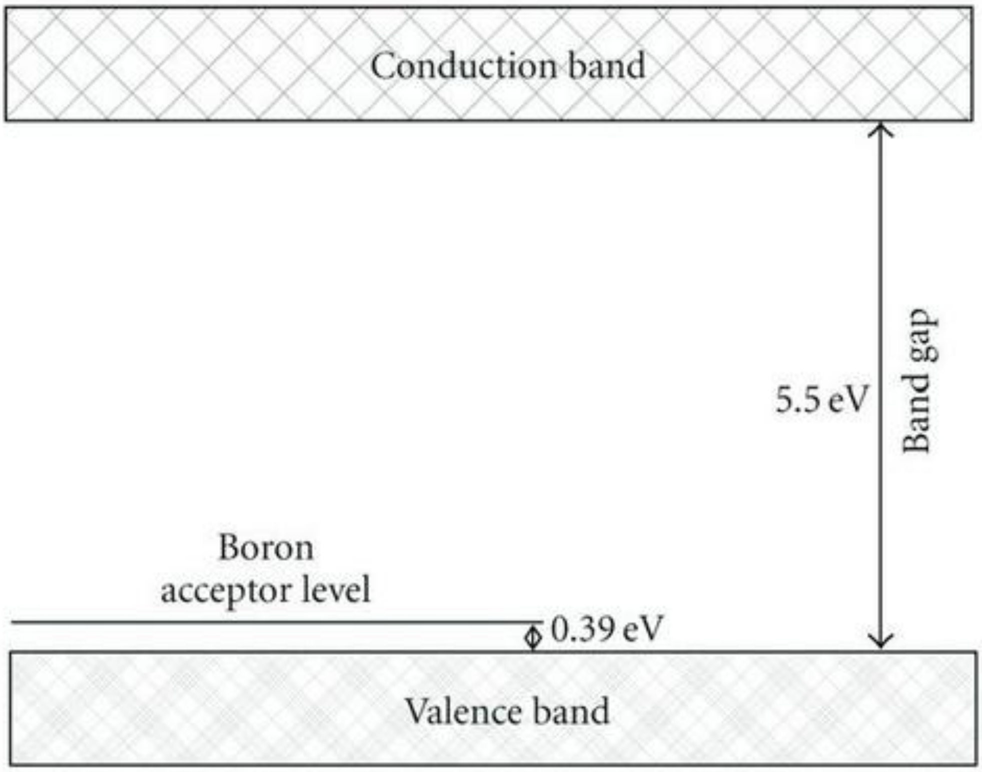

Figure 11 - A band gap diagram of BDD showing the boron acceptor level theoretically calculated by Wang and Zunger[37].

4.2 Surface Termination

Modification of the surface chemistry of diamond, such as oxygen termination, can alter diamonds work function, electron affinity, and surface homogeneity. The two methods of interest for oxygen termination include plasma and UV ozone treatment, each of which results in different surface coverage and properties[38]. Plasma oxygen treatment utilises high energy oxygen species (O_2 and O) in the gas phase under vacuum, to replace hydrogen termination via bombardment. This can damage and etch the diamond surface but also can remove graphitisation and fill vacancies. In addition, O-plasma treatment has been shown to raise the diamond work function by up to 1.6 eV. This is a result of surface dipole effects as the presence of electronegative oxygen groups attracts electrons and lowers electron density around the surface. The positive end of the surface dipole faces the bulk of the material and the negative end faces outward, this results in an increased energy barrier for electrons to escape the bulk material into vacuum – thus raising the work function[38, 39]. UV ozone treatment on the other hand, incorporates ozone into air in a contained space at room temperature and pressure under UV light to induce oxidation of the diamond surface. UV ozone treatment generally results in higher surface homogeneity and is lower energy, thus reducing surface damage. Similar to O-plasma treatment, ozone surface termination has been shown to increase the work function by approximately 2.1 eV. This can be explained by the increased presence of stable, electronegative carbonyl group surface termination. Current literature suggests that relative to a hydrogen terminated diamond, the rise in work function is correlated to the proportion of surface sites filled by oxygen functional groups due to the increasing surface dipole[38, 39].

After initial desired termination, the surface can be further terminated with metal. This technique is vital for the formation of Schottky diodes and, like oxygen termination, has multiple working approaches. The chosen method of deposition for this experiment was evaporation. This process involves the heating of the chosen metal under vacuum until it evaporates, it can then be condensed onto the chosen substrate.

5. Growth and Electrical Properties of Boron Doped Diamond

Inclusion of diborane in the gas precursor leads to the growth of BDD. This layer can be described as a p-layer when grown in MPCVD due to the positive charge effect created by the introduction of electron holes. Boron, with one less valence electron than carbon, can relatively easily occupy the same lattice positions as a carbon atom, and has a low activation energy[37]. As a result of this, high doping levels are possible, enabling conduction and making BDD a focal point in carbon electrochemistry[40].

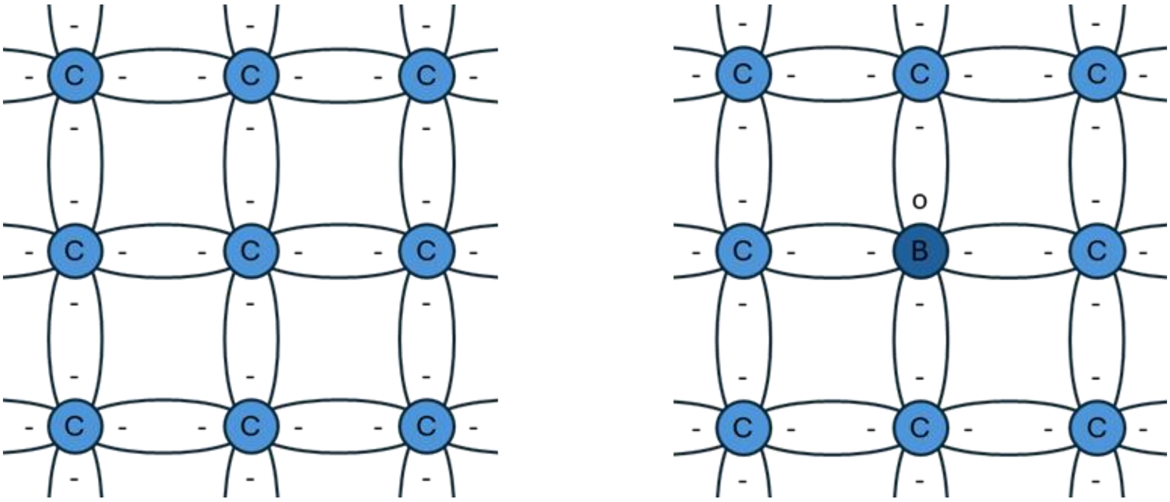

Figure 12 - A diagram showing the valence electron arrangement in i-diamond (left) and p-diamond (right). The electron hole present in p-diamond creates a free charge carrier which converts diamond from an insulator to a semiconductor. Figure adapted from Boylestad and Nashelsky[41].

The semiconducting nature of BDD alone is not enough to elicit major interest from electrochemists. It is this property in conjunction with diamond's ultra-wide bandgap, high carrier mobility (~2000 cm^2/Vs), thermal conductivity (2000 $Wm^{-1}K^{-1}$), resistivity

($1\text{x}10^{16}$ Ωm), and electric breakdown field (>20MV/cm) that make diamond a speculated holy grail in the world of semiconductors[11, 14, 15, 42].

Wide band-gap materials, like diamond, are generally more radiation hard and have a higher maximum conversion efficiency compared to lower band-gap materials[43, 44]. These properties set diamond apart from other highly popular semiconductors such as GaAs and silicon.

6. Betavoltaics; function and properties

6.1 Semiconductor junctions

Betavoltaics fall under the group of radiovoltaics; a device which generates an electrical current upon excitation by radiation from a radio-isotopic source. While gamma and alpha voltaic cells have been created, their use is currently limited due to the higher penetration or energy of the radiation, which causes greater material challenges and safety concerns[45, 46].

More recently, some scientists have experimented with liquid materials in an attempt to harness the power of alpha voltaics, where a semi-ordered liquid semiconductor exhibits self-healing effects to cope with the highly ionising radiation[47]. Despite the promising power outputs of alphavoltaics, beta cells remain the simplest and most studied form of radiovoltaic.

Betavoltaic cells, at a fundamental level, operate in the same way as a photovoltaic cell. In the case of betavoltaics, it is a beta particle (high speed electron) emitted from a radio-isotopic source, which takes the place of a photon to generate a current. When the beta particle successfully collides with the semiconductor, an electron from the valence band is excited into the conduction band, creating an electron hole pair. In many semiconductors, a pn junction can be formed where a p-doped substrate comes into intimate contact with an n-doped region. For current high performing semiconductor diodes such as gallium nitride, a p region can be formed by magnesium doping and an n region can be formed via silicon doping. The combination of these positively and negatively doped sections of substrate creates the aforementioned pn junction resulting in a depletion region. When electrons reach the depletion region, they are driven into n type side of the junction and holes are driven into the p type side, this is a result of the built-in potential of the junction.

Since the dawn of lab grown diamond techniques, the development of n-type diamond has been a problem studied meticulously by scientists throughout the field. Two key elements, nitrogen and phosphorous, have dominated scientific research over the last decade, however they are limited by deep lying donor levels and lattice structure restraints, respectively. To work around these issues, the diamond Schottky barrier diode has grown in popularity, however it does not come without its own set of limitations and challenges. Schottky contacts, which are relatively easily and cheaply produced are made by depositing a Schottky metal onto the diamond surface.

6.2 Metal semiconductor junctions – Schottky diodes

Upon contact formation between a metal and semiconductor, the fermi levels of the two materials equilibrate. Equilibration results in the formation of a Schottky barrier, which can be described as a potential energy barrier between the semiconductor and the metal. For a numerical description, the Schottky barrier height (which is dependent on the types of metal and semiconductor used), can be described by the Schottky Mott rule which states that:

$$\Phi B_p = E_g + \chi - \Phi_m \tag{1}$$

Where ΦB_p, E_g, χ and Φ_m are the barrier height, semiconductor band gap, semiconductor electron affinity and the metal work function, respectively.

The combination and equilibration of a metal and semiconductor energy bands can be visualised clearly in an energy band diagram:

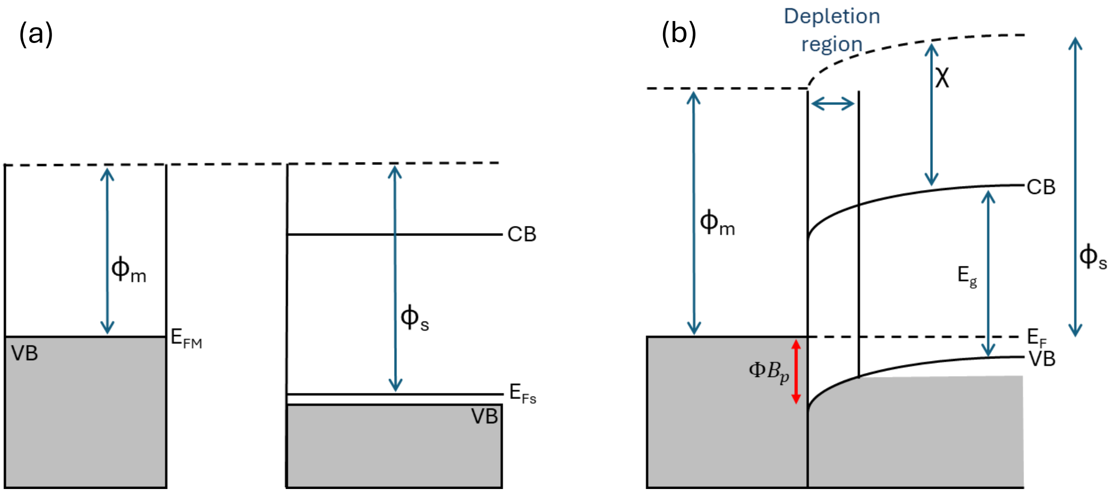

Figure 13 - Energy band diagrams of metal and a p-type semiconductor (a) before and (b) after equilibrating in a Schottky junction.

In a Schottky junction, the equilibration of the fermi levels between the metal and semiconductor leads to band bending in the valence and conduction bands of the semiconductor. The band bending generates a depletion region, devoid of mobile charge carriers, which establishes an internal electric field opposing further carrier movement. The key role of the depletion region is the diffusion of holes from the semiconductor into the metal, and conversely the movement of electrons from the metal into the semiconductor[48, 49]. This leads to charge separation at the interface, generating an internal electric field thus inhibiting further charge carrier diffusion after equilibration – this defines the built-in potential.

When a beta particle reaches the depletion region with significant energy, it can create an electron-hole pair. The built-in potential of the junction leads to separation and transportation of the charge carriers, preventing recombination and generating a measurable current. This is the fundamental mechanism for operation of Schottky barrier diode betavoltaics.

The most common design of the Schottky diode is a vertical structure as it demonstrates low series resistance, however expensive fabrication techniques have generally slowed down the production of this device[50]. Work by Bormashov *et al*. has successfully used ion beam assisted lift off techniques to generate ultra-thin film single crystal diamond Schottky diodes, this work highlights the cutting edge of diamond Schottky barrier diodes, and has shown significant early stage success in the series combination of these diodes to generate a functioning betavoltaic battery[44, 51].

Under a forward bias, when the Schottky contact is connected to the negative terminal and the p-diamond is connected to the positive terminal, there is a reduction in the built-in potential barrier. Application of a forward bias reduces the energy gap between the metal fermi level and the semiconductor valence band edge, resulting in decreased band bending in the valence and conduction band, this allows greater flow of electron holes from the p-type diamond into the metal thus increasing the current of the device. Reverse bias has the opposite effect; by swapping the negative and positive terminals the built-in potential barrier grows and band bending increases as a result of an increased energy gap between the fermi level and semiconductor valence band edge. The effect of this on carrier transport is reduced hole flow from p-type diamond to the metal, thus decreasing the device current.

Many different metals can be used to form a Schottky contact (Al, Pb, Ni, Au etc.), the effect of altering the metal is a change in barrier height[52]. This has been shown to have a direct impact on device function; increased barrier height leads to a lower leakage current and greater forward drop voltage[52].

Recent works suggest the Schottky barrier height could be the key to improving beta cell operation, as it is potentially linked to the open circuit voltage of the device which is an important factor in device efficiency[44, 53]. To change the Schottky barrier height, the work function must be changed for either the semiconductor or the metal. As previously described, this can be done for the metal by changing the chosen metal element deposited, in the case of diamond the work function can be altered either by changing surface termination or changing the dopant concentration. Multiple studies have been conducted attempting to optimise device composition and Schottky barrier height, this takes into consideration doping concentration, operating temperatures, Schottky metal, and operating voltage in order to minimise leakage current (increase efficiency)[54]. Aluminium is currently understood to produce the highest Schottky barrier when in contact with diamond, however it exhibits lower stress resistance and rectification than other metals such as chromium[55-57].

Another factor to consider for the power output of a beta voltaic device is the chosen radioisotope. Different radioactive materials will emit beta particles at varying rates and energies; for example, nickel-63 at ~18 keV and strontium-90 capable of emitting beta particles at energies up to 546 keV[58, 59]. These factors are massively important for determining device size, scalability, and potential device decay. Nickel-63's comparatively low energy beta emissions make it ideal for small scale devices as less material is needed to absorb the beta particles produced. An additional safety consideration for the use of radioisotopes in betavoltaics is the decay chain of the given compound. For example, safe options such as nickel-63, carbon-14, and tritium decay into stable copper, nitrogen, and helium, respectively. These isotopes will not contribute to further device degradation or health risk. The same, however, cannot be said for promethium-147 which decays into samarium-147, an alpha emitting radioisotope which could potentially degrade the device or pose user health risks.

7. Current State of the Art

The general consensus in modern literature is that a successful, high efficiency diamond Schottky diode needs a large Schottky barrier height to maximise device efficiency and limit leakage current[54]. Recent research has investigated the importance of drift layer thickness and boron concentration, with theoretical, high breakdown voltage devices operating with a doping level in the order of 10^{15} cm^{-3} and a thickness > 30 μm. However, it should be noted this device focuses on a punch through design with minimal ON state resistance[60]. Other contrasting experimental research has produced significantly slimmer drift layers (1-500 nm) with high levels of success, this research credits the success of thinner devices to the lower defect density in a thinner device[61]. Betavoltaic devices are not limited to diamond-based diodes – in fact other wide band gap semiconductors are more studied, developed and easier to produce than their diamond counterparts. For example, the first betavoltaic was reported by Paul Rappaport in 1954 using germanium and silicon, reporting a modest energy conversion 0.2%[62]. After 70 years of research and development on betavoltaic devices composing of mainly silicon and gallium compounds, maximum device efficiency has gradually plateaued in research. For instance, recent GaN pn junctions have reached a conversion efficiency greater than 26% which is less than 2% from the devices theoretical maximum[63]. In contrast, research in the infancy of diamond betavoltaic devices has surpassed multiple areas of electrical properties compared to non-diamond counterparts, such as conversion efficiency, power outputs and device lifetime. According to the Shockley-Queisser efficiency limit, a diamond based diode can reach a conversion efficiency of 34%, this provides plenty of scope for development from the current state of the art diamond pn diode which already resides at an impressive 28%[64]. The current commercial market is dominated by silicon and silicon carbide (SiC) devices over diamond and even GaN derived products. In the case of gallium nitride, which exhibits far superior qualities in terms of Baligas figure of merit, production is limited by high quality epitaxy with only a few reports able to produce low defect high performance devices[65]. Diamond devices are similarly stunted due to difficulties in high quality epitaxy; however, it could be argued the key constraint for diamond diodes and betavoltaic devices is high cost and low demand. At present, in the commercial market, diamond growth and device fabrication presents an immensely compromising ‘cost to performance’ ratio, with SiC devices performing too well to justify major investment for unrequired performance enhancement provided by diamond.

8. Project Aim

The aim of this project is to design, fabricate, and characterise a diamond based Schottky diode by harnessing microwave plasma-assisted CVD and its ability to produce high quality, controlled, doped layers of diamond. The ability to produce repeatable diamond based Schottky diodes has been recently documented in literature, however research is still limited in terms of optimal device structure and composition. This work could stand as a further benchmark and comparison to other devices, and help with the complex ongoing work to determine the ideal metal type, dopant concentration, drift layer and thus Schottky barrier height to make the highest performing Schottky barrier diode possible.

9. Method

9.1 Device Architecture

For the purpose of this thesis, two major device architectures were investigated with a third option noted for further consideration. These are vertical, free-standing vertical, and pseudo-vertical, respectively. The composition of these devices is as follows:

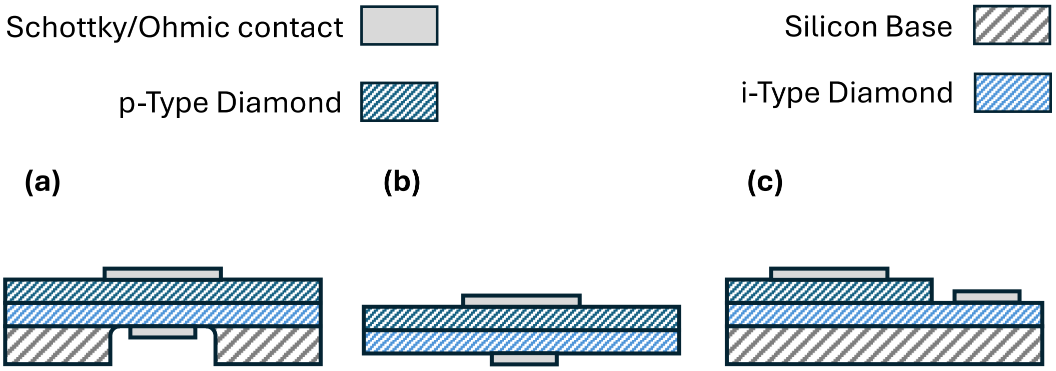

Figure 14 - Cross sections of the vertical (a), free-standing vertical (b) and pseudo-vertical (c) Schottky diode structures.

In the case of structure (a) and (c), a thin sheet of silicon (~700μm) acts purely as mechanical support to limit the fragility of the thin CVD diamond film. To increase the mechanical strength of device (b), a greater layer thickness is required and that may affect device efficiency[60, 61].

9.1.1 Device fabrication – Architecture (a)

For design (a), an initial silicon substrate was manually abraded using diamond powder. This process seeded the silicon surface with nanodiamond crystals, and increased the surface area which provided ideal conditions for heteroepitaxial polycrystalline diamond growth. The manually abraded silicon surface contains microscopic diamond seeds implanted in the surface which act as a nucleation site in CVD. Five structures were produced in an Applied Science and Technology (ASTeX)-type MPCVD reactor following the device standard operating procedure – for the purpose of this thesis I will refer to this as the back reactor. The back reactor is dedicated to boron doped diamond growth runs, as boron is highly contaminating, this means that even with diborane flow off the film will still have some boron doping. The benefit of this is that another ASTeX type reactor, the front reactor, can be used for undoped growth allowing higher purity intrinsic diamond growth. For each growth, a sample was centred on a molybdenum disk, which acts as a substrate holder, on top of a 0.5 mm spacer wire in the centre of the back reactor. Mass flow controllers (MFCs) were used to control gas flow rates, and an initial lightly doped p^--layer was grown under the following conditions:

Table 1 - The growth conditions for an intrinsic/lightly doped p^- polycrystalline diamond layer on samples A1-A5, grown separately in the back reactor.

Sample	A1-A5
Pressure / Torr	100
Temperature / °C	850-950
Power / kW	1
CH_4 Flow Rate / sccm	12.5
H_2 Flow Rate / sccm	300
Emissivity	0.19
Time / Minutes	120-180

A p^+-layer was then grown on top of the p^--layer by the inclusion of diborane into the chamber. The flow rate of diborane was 0.7 sccm and the temperature ranged from 918-990 °C and shorter growth times of 60-130 minutes, the remaining variables were unchanged[i]. An initial plan of 60-minute boron doped diamond growth time was extended in hopes of increasing film mechanical strength. Sample A5 was grown with a boron flow rate of 0.4 sccm to see if lower boron concentration would improve device strength.

Two samples were developed using the front reactor and a bespoke hot filament CVD reactor. Due to concerns around initial design size impacting mechanical strength, 4 x 9 mm silicon wafers were cut using the Oxford laser and manually abraded with diamond nano powder to seed the wafer. The wafers were then placed together in the front reactor and an i-layer was grown under the following conditions:

Table 2 - The growth conditions for a ~15 μm intrinsic polycrystalline diamond layer on samples A6 and A7, grown together in the front reactor.

Sample	A6-A7
Pressure / Torr	140
Temperature / °C	998
Power / kW	1.4
CH_4 Flow Rate / sccm	12.5
H_2 Flow Rate / sccm	300
Emissivity	0.19
Time / Minutes	305

Due to the back reactor being unavailable for maintenance, the hot filament CVD reactor was chosen to grow the boron doped layer on samples A6 and A7. Three tantalum filaments were fitted into the reactor approximately 3 mm above the samples on the molybdenum growth stage which was isolated using ceramic beads. The chamber was

---

[i] It is important to note that diborane used in the experiment is stored as 5% B_2H_6 in hydrogen.

secured and evacuated to a base pressure (8.2 x10^{-2} Torr) overnight. The base plate was then pre-heated to ~150°C for 30 minutes to minimise residual gases in the chamber. The filaments were resistively heated to ~2000°C and MFCs were used to carry out a growth under the following controlled conditions:

Table 3 - The growth conditions for a boron doped polycrystalline diamond layer on samples A6 and A7 using the bespoke hot filament reactor.

Sample	A6-A7
Pressure / Torr	20
Current / A	4
Temperature / °C	2000
H_2 Flow Rate / sccm	200
CH_4 Flow Rate / sccm	2
B_2H_6 Flow Rate / sccm	0.7
Time / Minutes	300

A necessary step in the fabrication of design (a) was micro-machining using a high-power laser system (Alpha 532-XYZ-A-U System, Oxford Lasers) equipped with Cimita and ALPHACAM CAD software. The laser system allowed ultra-precise cutting of samples to produce diodes of a chosen design and could graphitise diamond surfaces if desired in order to improve current flow at the wire/surface interface.

A 2.5 x 1.5mm window was etched into the reverse side of the diode, initially with the Oxford laser followed by a heated wet etching sequence with 5-7M potassium hydroxide (KOH) and Kapton tape. The chips were laser etched at varying powers and speeds in a cross hatched pattern to reduce the likelihood of damage and maximise uniformity of the diamond membrane. A schematic of the laser etching process, along with an image of one of the samples can be seen below:

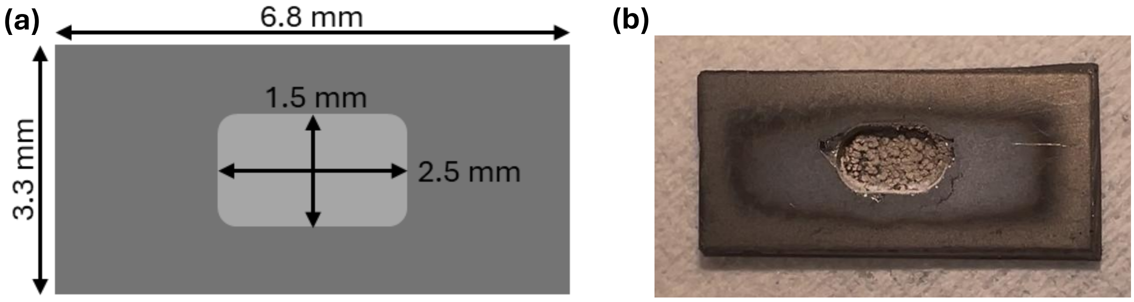

Figure 15 - (a) A diagram of samples A1-A5 showing the mentioned dimensions of the chip and recess and (b) an image of sample A6 after laser etching showcasing the change in surface appearance.

It is important to mention that after each laser etching process the sample was placed into a beaker containing a 1:1 mix of acetone and isopropyl alcohol and sonicated for 10 minutes. This process ensured clearance of debris built up during the etch.

The etching sequence for sample A3 can be seen below:

Table 4 - A comprehensive list of the etching sequence, including all necessary settings, used to laser etch sample A3 in the Oxford laser system.

Etch Number	**Power / %**	**Number of Passes**	**Speed**
1	30	6	4
2	30	4	3
3	30	8	3
4	40	4	3
5	40	7	3
6	40	4	3
7	40	6	4
8	45	4	3

To wet etch, the chips were masked in Kapton tape and placed in KOH at 80-90 °C to selectively etch the remaining silicon and expose the intrinsic diamond surface on the reverse face of the diode. This was repeated as many times as necessary to reveal a majority diamond surface in the recess, and the Kapton tape was replaced each time the etch was repeated. The setup for the wet etching process can be seen below:

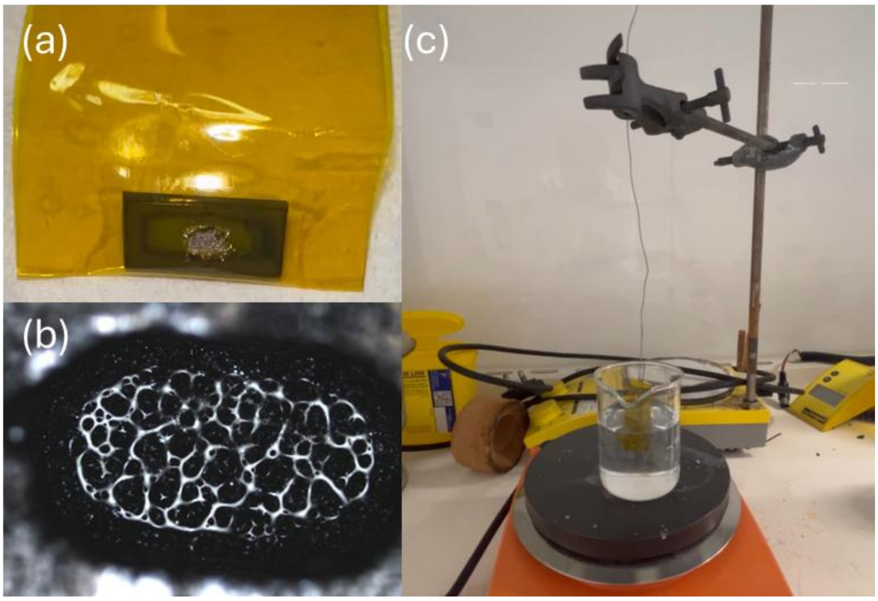

Figure 16 - Images of the wet etching set up showing (a) the Kapton tape mask applied to the sample with a selective hole cut to expose the laser etched recess, (b) LEXT imagery of the KOH etched recess in sample A3 and (c) the etching apparatus made up of a clamp, beaker, wire, 5-7 M KOH and a hot plate heated to 80-90 °C, a magnetic stir bar was also employed at 150 rpm however this is not included in the image.

For sample 3, the masked diode was submerged in 75 ml, 5 M KOH and heated to 80 °C. The solution was kept stirred for 1 hour at which point the Kapton mask had begun to deteriorate. After one hour of stirring, the sample was removed from solution and washed in deionised water and then acetone before a new mask was applied in the same way. This process was repeated until LEXT microscopy showed a majority flat diamond surface in the etched recess, for sample three this took 8 KOH etching sequences. The number of etching sequences varied for each production and was reduced upon change of solution from 5 to 7 molar KOH as well as an increase from 80 to 90 °C.

9.1.2 Device Fabrication – Architecture (b)

Structure (b) was the simplest design to manufacture, not only for its lack of surface preparation but also the fact it needs no major refining steps such as etching for design (a) or masking for design (c). As design (b) is made up only of freestanding polycrystalline diamond (i and p type) it requires only one of the free-standing sheets to be premade, from that point the process requires far fewer steps to reach completion than for design (a). A starting point of a free-standing Element Six BDD PCD (5.0 x 9.0 mm, boron concentration ~4 x 10^{20} atoms/cm^3), was chosen and a ~5-10 μm i-layer was grown across the whole surface in the front reactor under the following conditions:

Table 5 - The growth conditions for samples B1 and B2 to grow an intrinsic polycrystalline diamond on top of Element 6 BDD substrates.

Sample	B1	B2
Pressure / Torr	130	130
Temperature / °C	958	960
Power / kW	1.3	1.3
CH4 Flow Rate / sccm	12.5	12.5
H2 Flow Rate / sccm	300	300
Emissivity	0.15	0.15
Time / Minutes	90	180

9.1.3 Device Fabrication – Proposed Architecture (c)

Device (c) follows a process somewhat similar to design (a). To allow heteroepitaxial growth of diamond on silicon, a silicon wafer would be manually abraded using nano diamond powder. An initial i-layer of approximately 10 μm would then be grown before the CVD is halted so that a molybdenum mask can be applied. Diamond growth would then resume with the inclusion of diborane to selectively grow a concentrated p-layer with the silhouette shown in Figure 14.

9.2 Surface Termination and Metal Deposition

The following method was only applied to design (b) however the principle is identical for (a) and only differs by application of a selective mask for design (c).

Initially, the surface was terminated with oxygen using plasma termination. The samples were loaded into a modified sputter-coater (Edwards S150A) and subjected to O_2 DC plasma. This was carried out for 5 minutes at room temperature with a pressure of 1 Torr, a current of 48 mA, and oxygen flow rate of 10 sccm. This high energy process fills surface vacancies and removes graphitisation. The diodes were then oxidised via UV ozone treatment. The samples were exposed to UV light generated by a mercury lamp in the presence of ozone in a UVO-cleaner (Model 42, Jelight Company Inc.) for 30 minutes. The decomposition of ozone at room temperature generates reactive oxygen species, which readily react with the diamond surface to complete an oxygen monolayer.

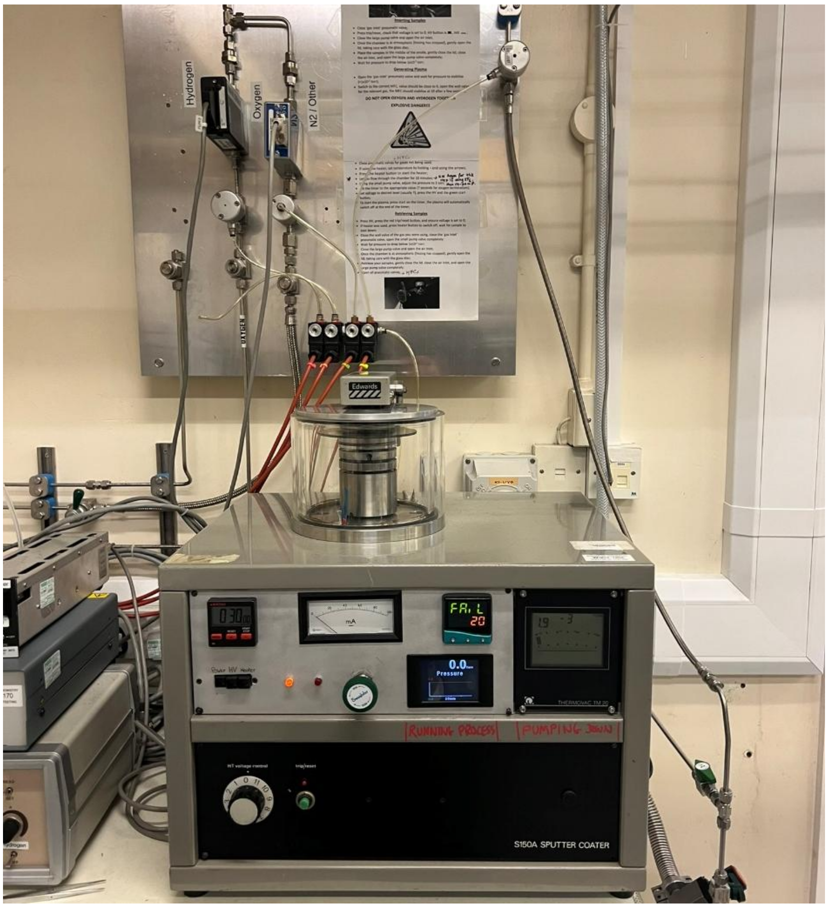

Figure 17 - The S150A Sputter Coater in the University of Bristol Diamond Lab. This sputter coater utilises oxygen plasma to terminate the diode surface in preparation for Schottky contact application.

Aluminium Schottky and ohmic contacts were then deposited onto the surface using thermal evaporation. Aluminium was evolved from a tungsten dimple boat at a base pressure of 8×10^{-6} Torr and heated until evaporation in a physical vapor deposition plant

(Balzers BA 510 coating plant). The sample was mounted in a calotte plate facing down approximately 40 cm from the evaporation source, and the aluminium layer thickness was measured to be ~100 nm with the Agar quartz thickness monitor (Agar AGB7448).

Figure 18 - The Balzers BA 510, a metal deposition machine that operates via vacuum evaporation[66]. A Balzers BA 510 can be found in the University of Bristol School of Physics building and can be used for deposition of a variety of metals, in this case it was used to deposit aluminium.

9.3 Metal Contact Connection

Silver dag was used to apply nickel-coated copper wires (150 μm diameter) to the aluminium contacts on the diode as seen in Figure 17. After successful application of the wire, the silver dag was left to dry overnight at room temperature to ensure the dag had set and the contacts had maximum stability.

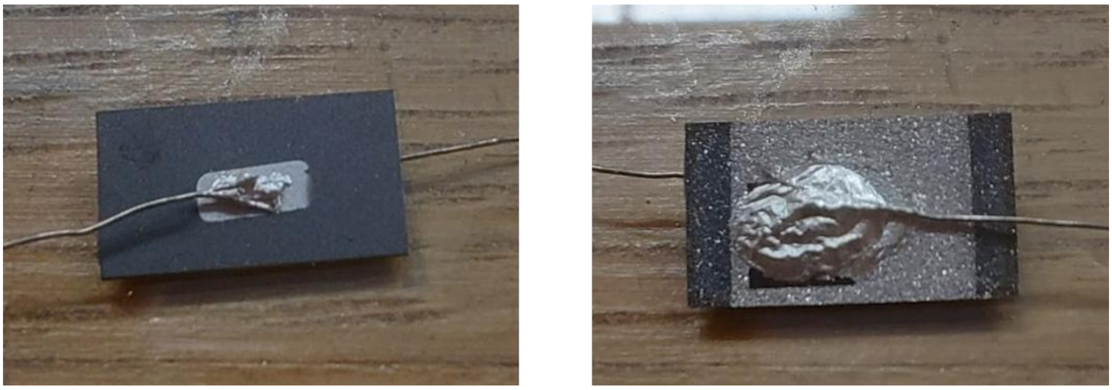

Figure 17 - The front and back face of sample B2, a smaller aluminium Schottky contact is deposited on the front (intrinsic) diamond and a small amount of silver dag was carefully applied. The ohmic contact on the boron doped diamond covered a larger surface area and so silver dag application was a less delicate process.

After initial I-V readings for sample B2 were weaker than expected, a graphite channel was etched onto the ohmic contact using the Oxford laser (50% power, etch speed 1 mm/s, 1 pass) in an attempt to increase the device current. The silver dag was reapplied in the same manner to the ohmic channel.

10. Characterisation Techniques

10.1 LEXT Imaging

Ultra-fast, high quality surface imaging and analysis is made possible by the LEXT microscope (LEXT OLS5000, Olympus). The LEXT microscope has a focal range from 5x to 100x zoom, and can take detailed images of the diode surface to assist other experimental evidence that provide results on surface defects and composition. In addition, it can accurately measure surface heights allowing for roughness approximations and layer thickness identification. The LEXT microscope was vital for etch depth analysis in the fabrication of diode (a) as it could show the height of silicon left after each laser etching sequence. To take measurements using the LEXT microscope, it was turned on and allowed to focus before the samples were loaded onto the stage. After the samples were positioned, a map was taken to aid the viewing process. In general, the samples were subjected to a 10-20x zoom surface depth analysis, in order to determine the difference in height between the top of the diode and the recess that had been etched. This height analysis took advantage of the LEXT's stitching function in which multiple areas of ultra-precise measurements could be connected in a continuous 3d image.

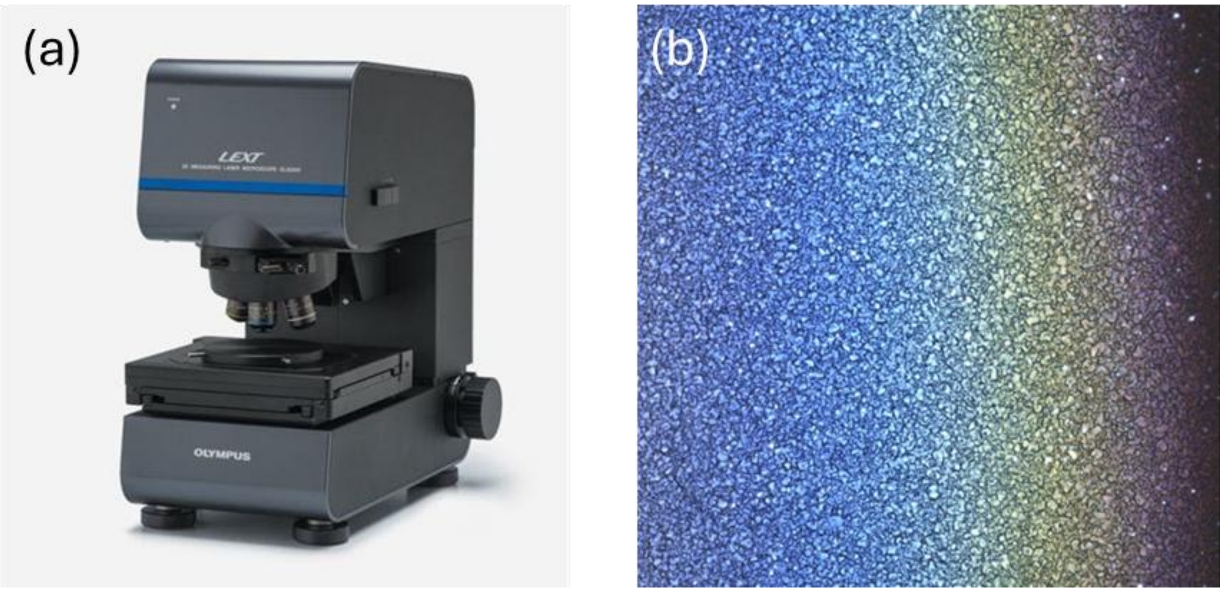

Figure 18 – (a) The LEXT OLS5000 microscope used to take sample profile measurements and surface images and (b) a rainbow effect on boron doped diamond caused by rapid cooling of the substrate after the back reactor was shut down quickly.

10.2 Raman Spectroscopy

The Renishaw SM2000 Raman Spectrometer is a useful tool for confirmation of the device's chemical composition. The spectrometer measures the inelastic scattering of light off a chosen sample which results in different energy photons; the change in energy is associated with the vibrational modes of the compound in the sample, and so each different structure will provide a unique spectrum. Pure single crystal diamond has a distinct Raman peak of ~1332 cm^{-1}, this value is a helpful benchmark for comparison to the diodes grown in this project. To take measurements, samples were placed onto the microscope stage and a green (514 nm) Raman laser was focused onto the surface of the diode. A spectrum was generated following the set exposure times and the results could be compared directly to the calibration spectrum produced by a sheet of intrinsic single crystal diamond.

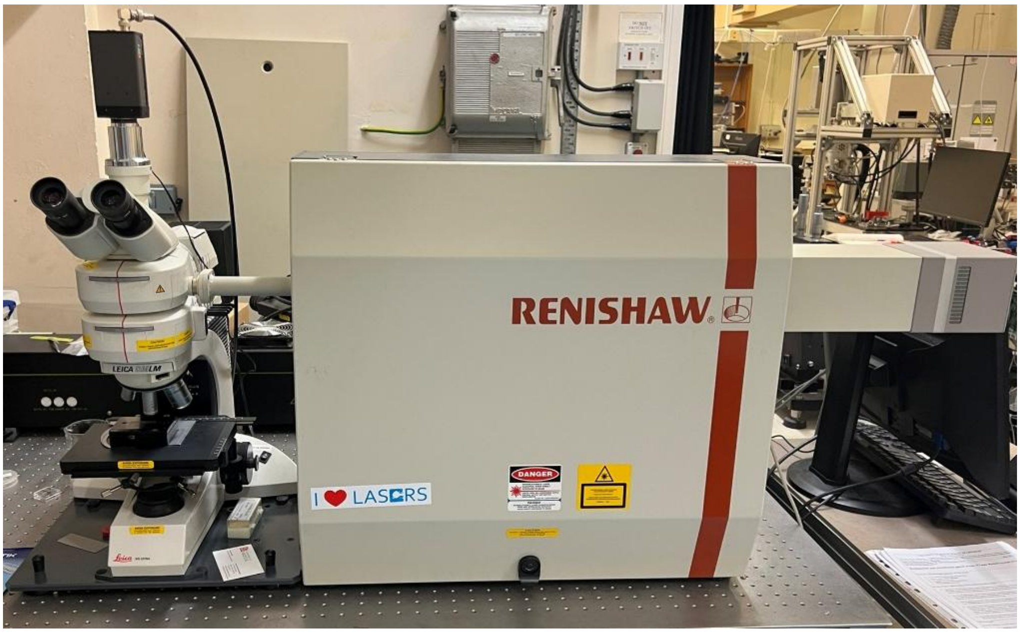

Figure 19 - The Renishaw SM2000 Raman spectroscope operated at a wavelength 514 nm; the spectroscopy was a useful tool for substrate analysis.

10.3 Keithley I-V Measurements

The Keithley source meter is an essential tool for measuring the current voltage characteristics of the diodes produced. The Keithley 2401 source meter has a voltage range of -20 – 20 V, meaning it allows low voltage diode characteristic tests through iterative current-voltage measurements. A second Keithley device (Keithley Electrometer, 6517A) was used for the same purpose but had a voltage testing range of -100 – 100 V allowing slightly higher power diode characteristic measurements.

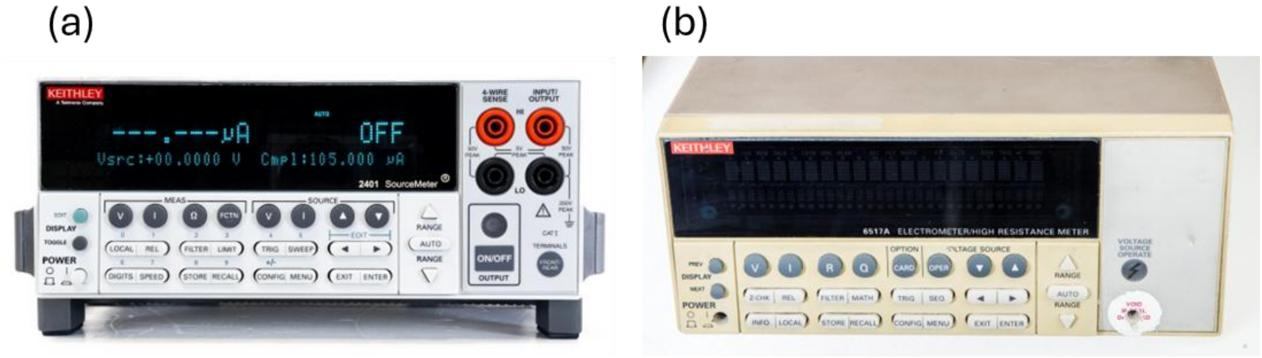

Figure 20 - The two Keithley devices used in the Diamond Lab. (a) The Keithley 2401, a source meter with a voltage range of -20 to 20 V used in initial IV tests and (b) the Keithley electrometer 6517A with a much larger voltage range of -100 to 100 V, used for IV measurements during e-beam tests[67, 68].

10.4 E-Beam Measurements

The electron beam system (EGF-3104 and EGPS-3104, Kimball Physics) can be used to simulate beta irradiation without the need for potentially harmful radioisotope sources. Electrons can be accelerated to simulate beta particles with energies up to 100 keV, more than enough to simulate a nickel-63 radioisotope source which emits beta particles with energy ~18 keV.

The e-beam anatomy is made up of 5 principal components:

- Triode
- Electron emitter
- Electrode and electric fields
- Anode and cathode
- Wehnelt Cylinder

The triode vacuum tube is the three-piece combination of a cathode, anode and grid, it is responsible for controlling the electron emission. Free electrons are generated at the cathode, these electrons are accelerated via attraction to the anode and are directed down the beam. The grid is responsible for controlling emission of the electrons from the cathode.

The electron emitter, as it sounds, provides the source of electrons in the e-beam and as previously mentioned, forms the cathode in the triode. The e-beam apparatus supporting this research uses a tantalum wire as the cathode. A low voltage is applied to heat the cathode resulting in emission of electrons at the surface, as some electrons reach sufficiently high energy to be released from the outer atomic orbitals of the cathode.

The electrons emitted from the cathode must then be directed to provide useful function, this process is controlled by the electric fields. These fields are generated by electrodes, which are separate to the anode and cathode, they manipulate the beam trajectory to a desired point.

The cathode and anode are responsible for the major electric fields generated by the e-beam. They are operated at a large difference in potential (e.g. -1000 and 0 V), causing the acceleration of electrons from the cathode in the direction of the anode.

The Wehnelt cylinder is the final major component of the e-beam and sits next to the cathode. It operates at the most negative potential in the e-beam and aids in direction of emitted electrons[69].

For current-voltage tests under electron irradiation, the desired sample could be mounted in the e-beam and connected to the Keithley 6517A. Electrons could then be accelerated to a specific energy and focused onto the semiconductor whilst the Keithley applied a bias and took current readings.

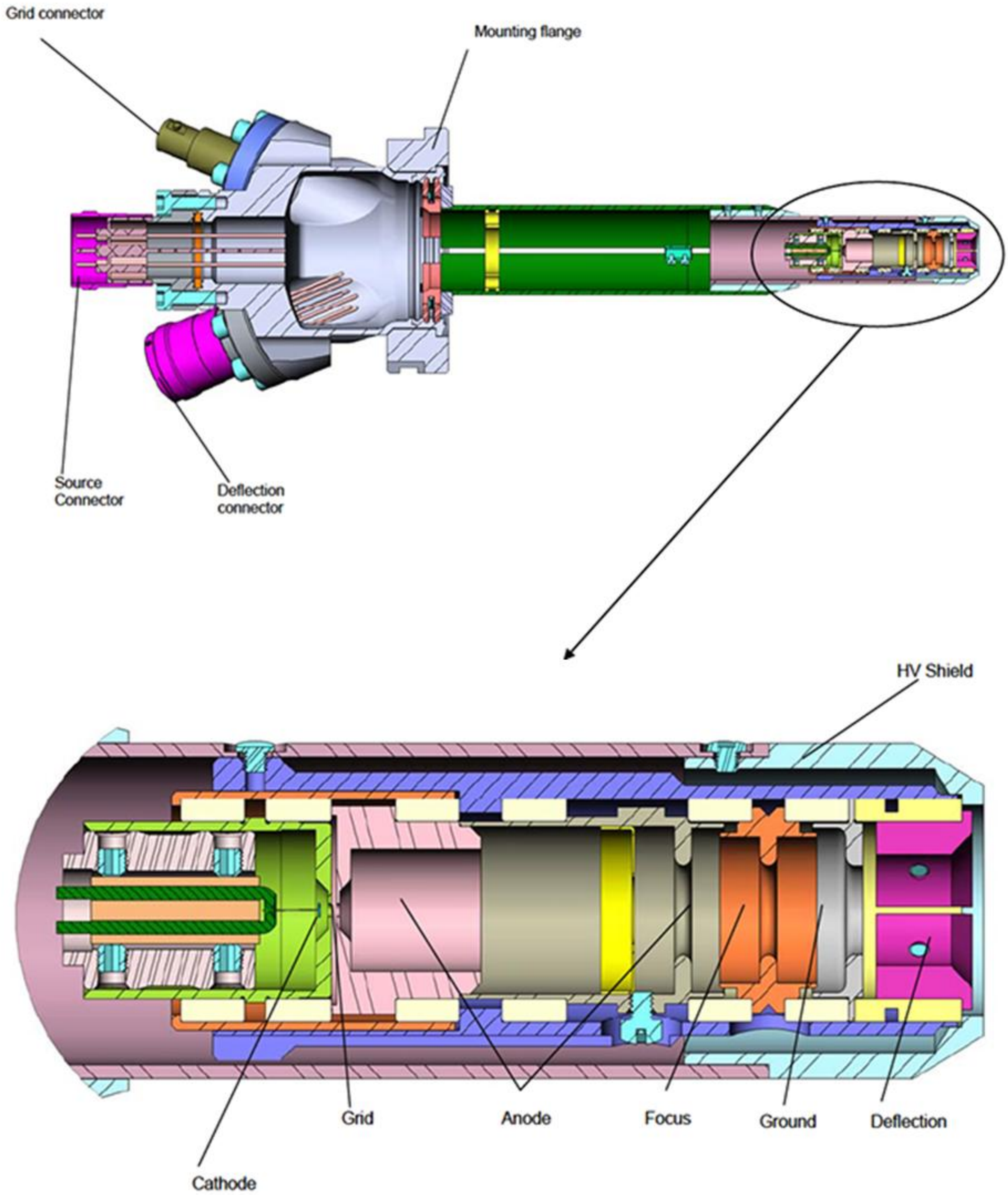

Figure 21 - A detailed schematic of the Kimball Physics electron gun used to simulate beta irradiation on sample B2[69].

11. Results

11.1 Raman data

The spectra from the Raman spectrometer confirm the presence of diamond, however generally the peaks are broad and contain a large sp^2 hybridised region highlighting the presence of graphitic, high defect areas. This is somewhat expected due to the lower quality and high grain boundary presence of polycrystalline diamond, however slightly sharper peaks and lower graphitisation were thought to be possible. The lower quality of some of the diamond is likely due to the residual concentration of boron within the back reactor as well as fluctuating temperature during growth.

The Raman spectrometer was also used to confirm the presence of diamond after the laser and KOH etching sequences.

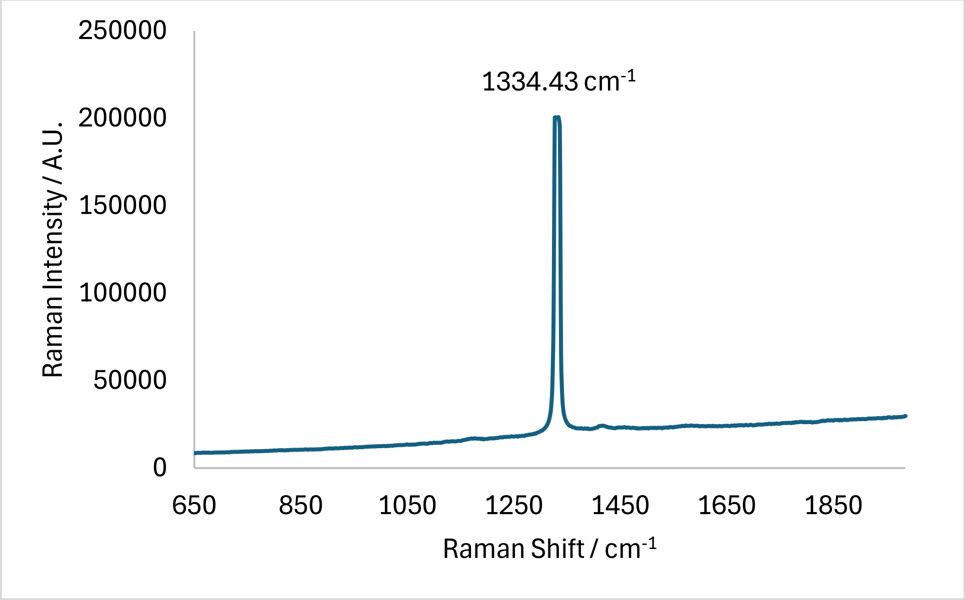

Figure 22 - The Raman spectrum for the calibration sample showing a distinct peak at 1334 cm^{-1}

The calibration spectrum shows a small red shift with a peak at 1334 cm^{-1}. While this is slightly shifted from the expected 1332 cm^{-1} it is still a perfectly reasonable calibration and is likely caused by sample stress or surface impurities. The distinct peak is typical of the A1 diamond stretching mode, in which all atoms move in phase.

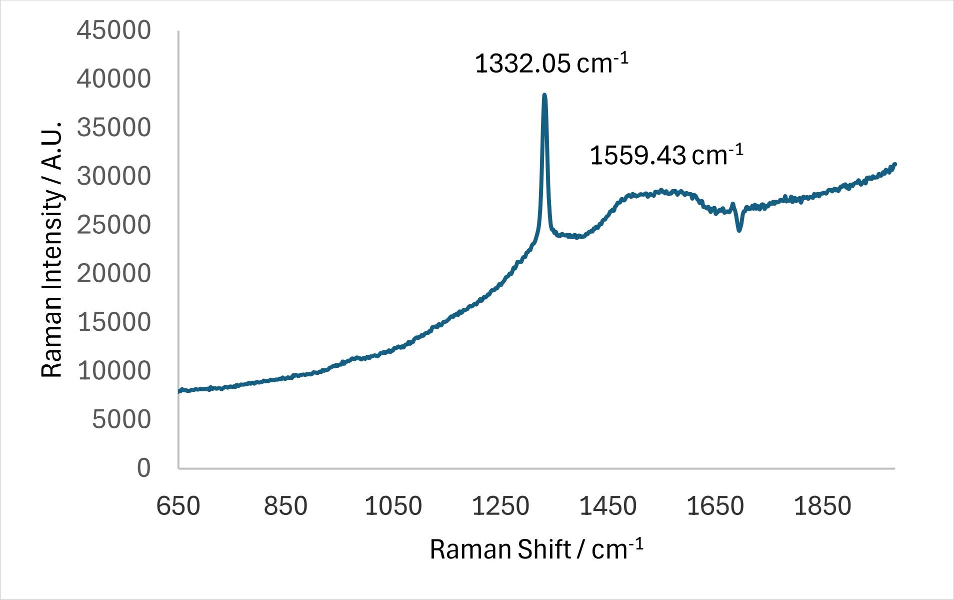

Figure 23 – A Raman spectrum for intrinsic polycrystalline diamond. This sample was grown separately from the diode chips whilst attempting to optimise gas flow rates for diamond growth however it now stands as a secondary useful benchmark for polycrystalline CVD films grown throughout the project.

The intrinsic diamond film exhibits the expected distinct diamond peak at 1332 cm^{-1} however it also now displays a notable peak around 1550 cm^{-1}. The new peak at a higher shift is denoted as the G band, referring to regions of sp^2 hybridised carbon which is expected in polycrystalline diamond due to graphitisation, and amorphous carbon defects found in the grain boundaries.

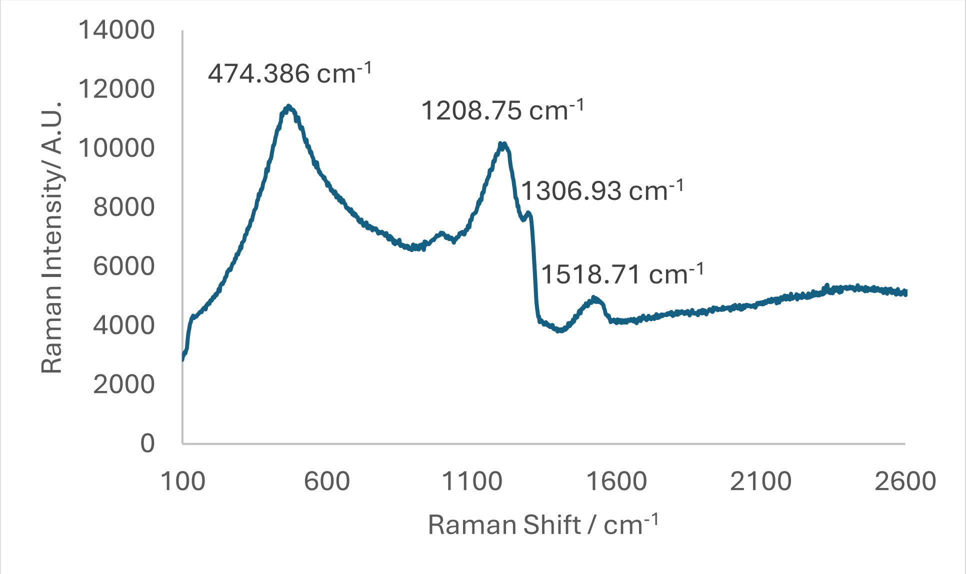

Figure 24 - The Raman spectrum of sample A5, a polycrystalline boron doped diamond. The spectrum has 4 major peaks of interest which tell us about the content of the CVD diamond.

The introduction of boron into the diamond lattice results in local vibrational modes at lower Raman shifts. Heavy boron doping is agreed to be directly responsible for the peaks observed around 474 cm^{-1} and 1208 cm^{-1}, however literature debates the origin of the of the former peak as it is not definitive of either B-B or B-C bonding[70]. The latter of the two mentioned peaks is more confidently understood to be a C-C vibration. The diamond Raman line has been noticeably blue shifted and displays an asymmetric peak, this has been described as the Fano effect. This is an interaction between discrete phonons and a continuum of electronic states, which results in a Raman peak with asymmetric character[71]. The remaining peak at ~1500 cm^{-1} is symbolic of a graphitic G band.

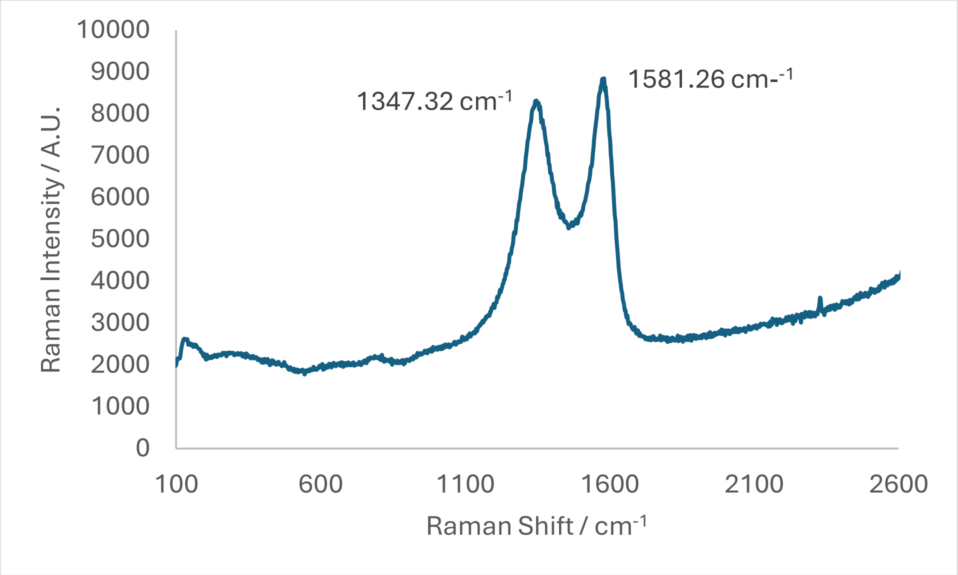

Figure 25 - The Raman spectrum of sample A6, showing two distinct peaks, the D and G bands of graphitised and amorphous carbon.

Samples A6 and A7 showed disappointing (and identical) Raman spectra. Both were dominated by the presence of a D and G band around 1350 cm^{-1} and 1585 cm^{-1} respectively. Both samples were grown together with a boron doped layer produced in the hot filament CVD reactor; however, this spectrum suggests minimal boron presence and extremely high levels of graphitisation of the substrate.

11.2 LEXT Microscopy

The LEXT microscope provided precise depth measurements vital for tracking the etching process of device architecture (a). Typically, a measurement was taken after each etching iteration unless it was visibly evident minimal depth change had occurred.

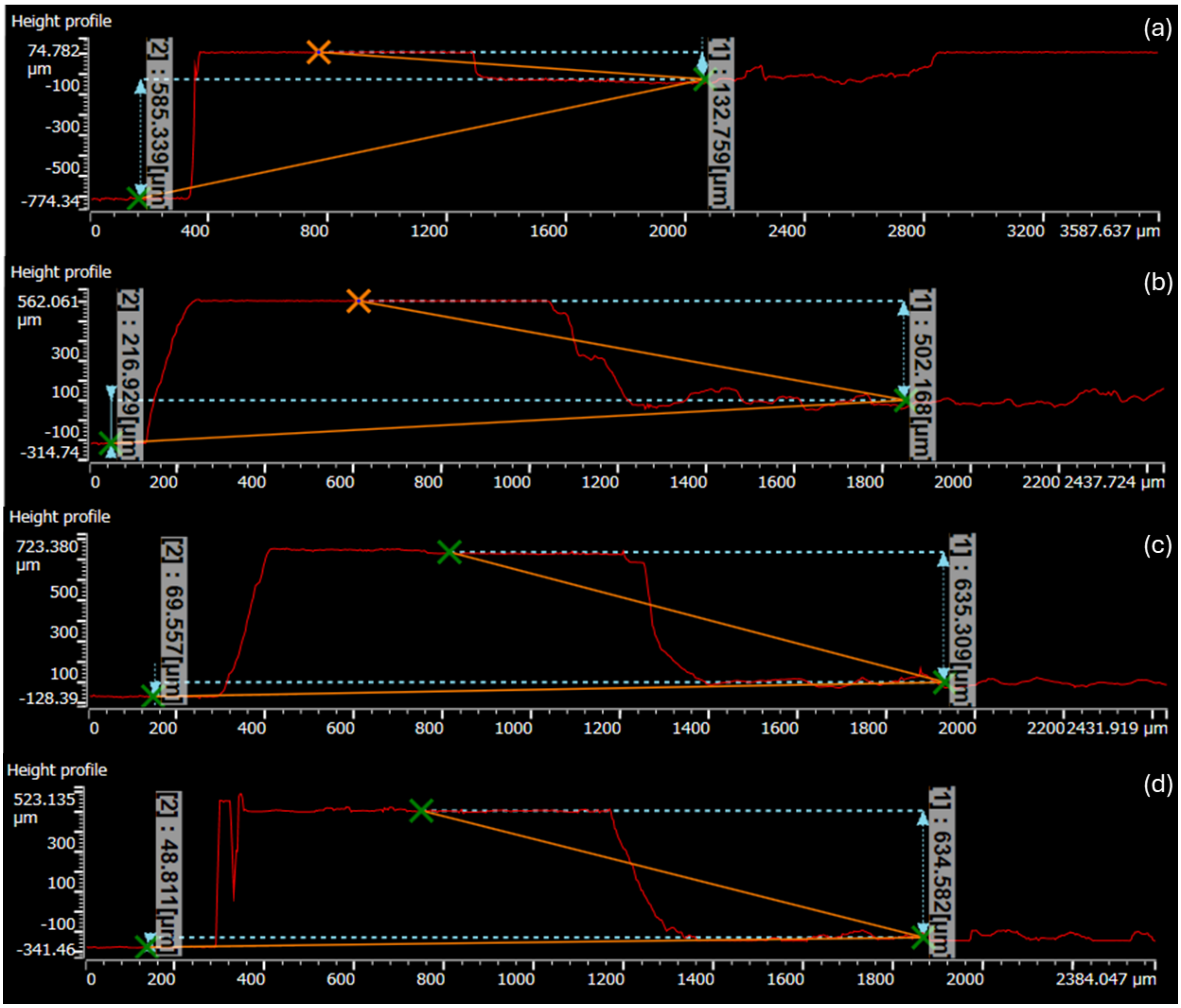

Figure 26 - Profile measurements of sample A3 after (a) the first laser etching sequence, (b) the final laser etch, (c) the first KOH wet etching sequence and (d) the final wet etching sequence when sample A3 was determined to be ready for metal contact application.

Table 6 - A table of etching heights after the initial and final laser and wet etching. The table directly quantifies the etching values recorded in Figure 26. An approximate etch height was used to account for loss of silicon after deterioration of the Kapton mask.

Etch Number	**Etch Depth / µm**	**Height to base / µm**	**Approx. Total etch height / µm**
Laser 1	135.76	585.34	135.76
Laser 8	502.17	216.93	502.17
KOH 1	635.31	69.56	654
KOH 8	634.58	48.81	670

LEXT data evidenced a particularly arduous fabrication aspect of design (a), that being inconsistent etching rates by either laser or wet etching. The rate of etching was hard to predict due to the anisotropic arrangement of the silicon wafer. Different crystallographic orientations (111, 110, 100) exhibit distinct surface atomic densities which directly impacts etching rates. For wet etching, literature experimental data has confirmed slower etching rates for (111) planes compared to other orientations. The calculated etch rates were generally in agreement with the observed variability in our experiments[72].

Along with the varying etch rates caused by different surface orientations, this thesis proposes that high energy laser ablation of the silicon can in some instances lead to surface oxidation. This would account for the built up of white, brittle irregular structures within the etching recess during the procedure that caused further difficulties in the production of the diamond membrane.

11.3 IV Data

Of the two devices produced, sample B2 showed diode characteristic, whereas B1 appeared to be an insulator within the Keithley voltage range. The recordings measured by the Keithley source meter were highly changeable based on the application of silver dag to connect the wires and metal contacts. Because of this, multiple measurements were taken after repeated removal and reapplication of the silver dag in an attempt to discover maximum device functionality.

11.3.1 Diode B1

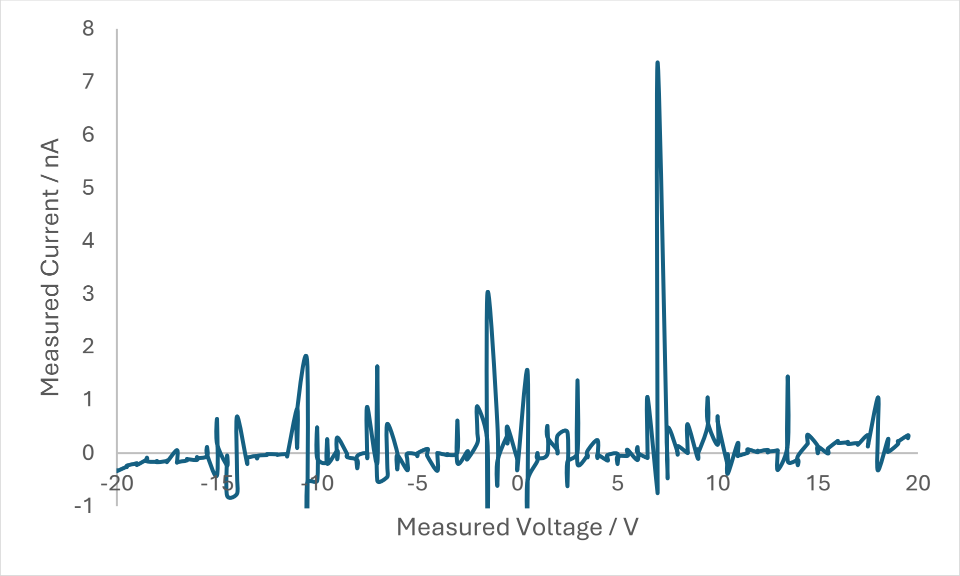

Figure 27 - Current-Voltage characteristics of device B1. The device appeared to act as an insulator, giving no measurable IV characteristics between -20 and 20 V. The varying, low magnitude, current readings are simply noise from the Keithley 2401.

After 3 attempts to reapply the silver dag on B1 with recurring unsuccessful results it was decided to discontinue further IV tests so that diode B2 could be optimised in a short space of time.

11.3.2 Diode B2

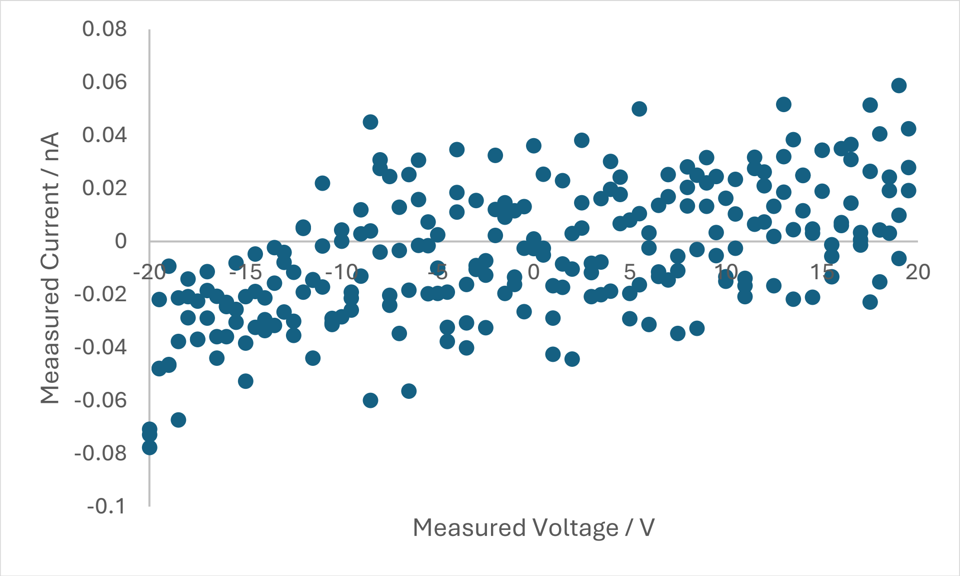

Figure 28 - Initial current-voltage characteristic readings for sample B2. The near picoamp magnitude of current across the voltage range and shape of graph suggests insulator characteristics.

As previously stated, the diodes gave varying current-voltage responses that appeared highly sensitive to quality of contact made by the silver dag and wire. Optimising the application of silver dag perhaps by the use of more refined equipment would likely improve consistency and performance of the devices.

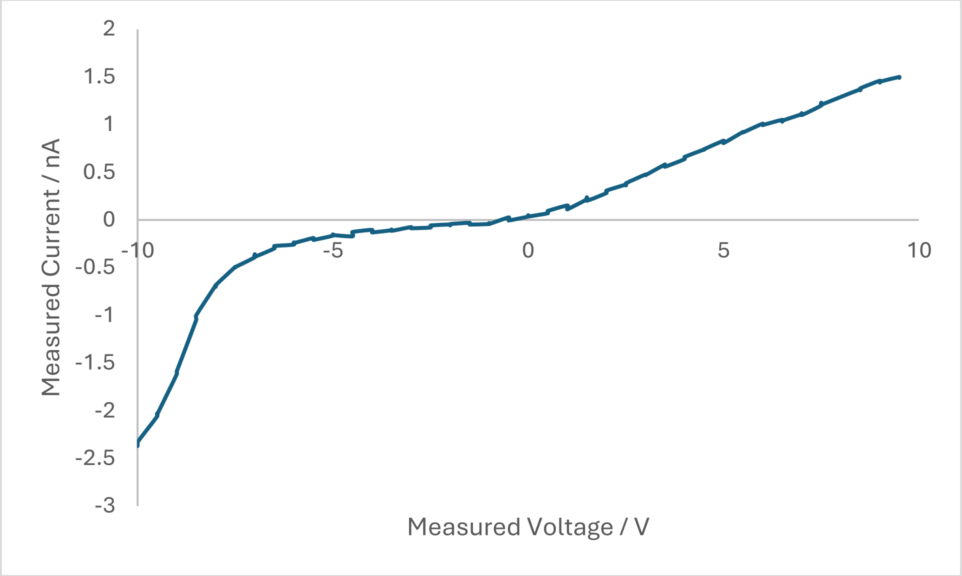

Figure 29 - Current-voltage recordings of sample B2 showing some diode characteristic with what appears to be a high leakage current and ON voltage.

The IV graph of B2 showed promise with distinct diode characteristics demonstrating an ON voltage around -7.5 V however reverse leakage current was relatively high leading to a rectification ratio of approximately 1.67 at 10 V. This rectification value is incredibly low compared to other diamond Schottky diodes reported in literature and is the result of high leakage current and low forward current voltage rather than either individually.

11.4 Electron Beam IV Data

Device B2 was measured before, during and after exposure to the E-beam. Whilst in the e-beam, the diode was subjected to four magnitudes of electron energy: 5.6, 10, 15 and 20 keV. The average energy of a tritium beta particle is 5.6 keV thus the lowest mentioned energy test on the e-beam is an ideal simulation of tritium decay. During the e-beam run, the diodes were subjected to a current-voltage test with a magnitude of 100 V using the Keithley 6517A, this test would simulate the response of the diode to beta irradiation from different radioisotopes.

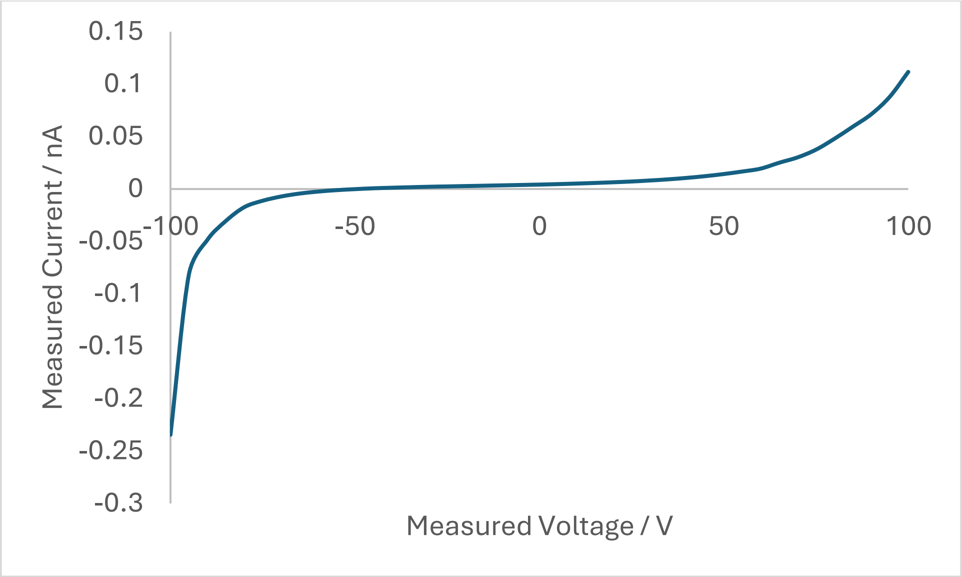

Figure 30 – The pre-beam current-voltage measurement for diode B2 between -100 and 100 volts.

After reapplication of silver dag, diode B2 exhibited a lower current between a voltage range of -100 and 100 volts than it displayed on the shorter range applied by the Keithley 2401. While the reduced current is disappointing the rectification ratio did increase from ~1.6 to ~2.1 suggesting a slightly improved device efficiency.

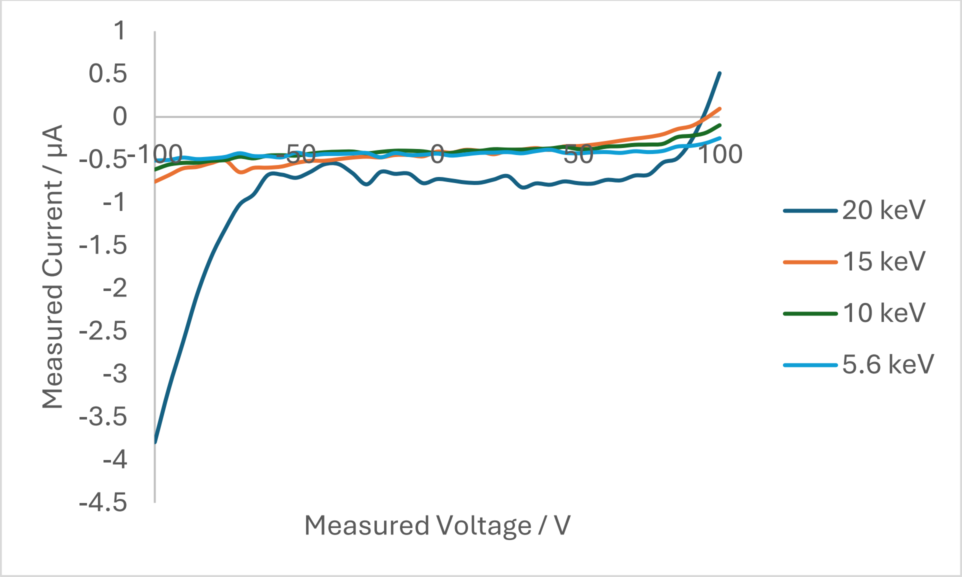

Figure 31 -The in-beam current-voltage measurement for diode B2 between -100 and 100 volts. The diode was irradiated by electrons with varying energies simulating exposure to beta particles with energies similar to that of tritium and nickel-63 isotopes.

The in-beam measurements showed low variability for <15 keV electron irradiation. The current range across the total bias was approximately 0.6 µA for the 10 keV test and varied only slightly for 5.6 and 15 keV runs.

Conversely to the lower energy tests, irradiation with 20 keV electrons showed significant performance boosts with a rectification ratio close to 6 at 100 V, and a current 3-4 orders of magnitude larger than that for the pre-beam test.

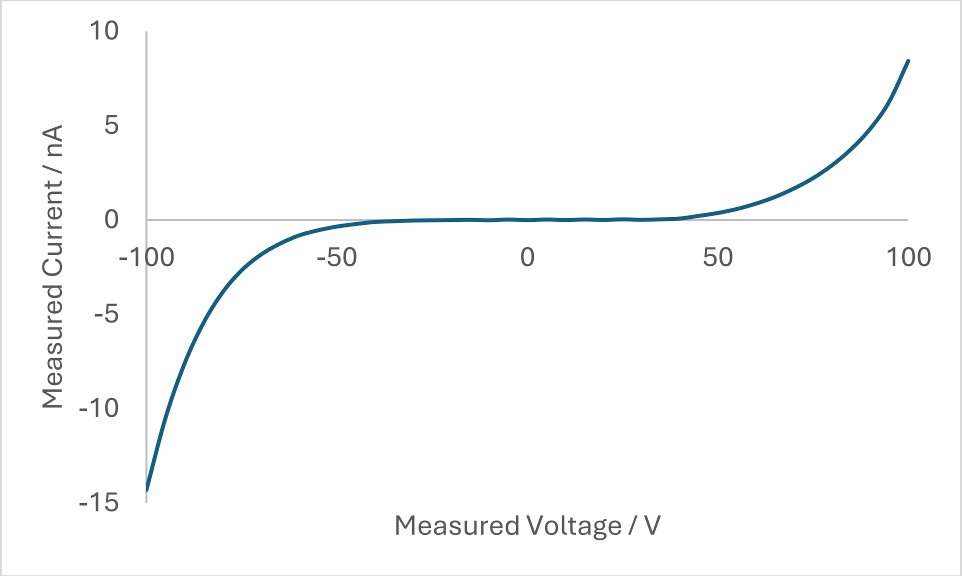

Figure 32 – The post-beam current voltage measurement for diode B2 between -100 and 100 volts.

The post beam analysis showed a current an order of magnitude greater than the pre-beam test. This apparent activation is likely the result of residual charge carriers, however SEM and XPS imaging before and after the tests could have provided further insight into any structural changes.

11.5 Beta Particle Irradiation Tests

Although device B1 did not present any diode characteristics after initial IV tests using the Keithley source meter, it was selected to undergo beta irradiation to see if any charge collection was occurring. When subjected to potassium-40 beta irradiation, which has an average energy of roughly 0.5 MeV, strong unipolar beta pulses were detected for individual beta particles using a Cremat-based detector (TDS 210, Tektronix). The detector elongates the measurable response to the beta particle and shows its unipolar nature, which is significantly different to the sinusoidal response created by noise.

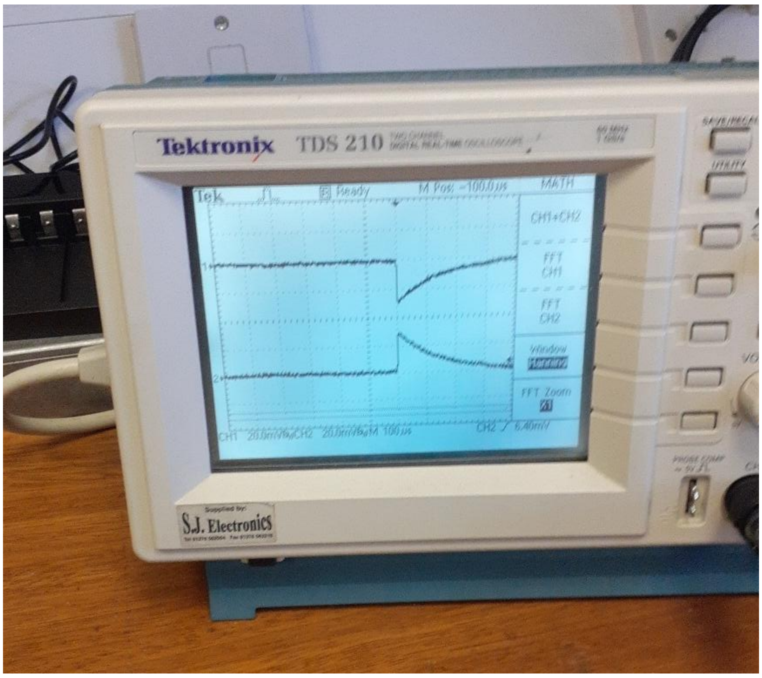

Figure 33 - An individual beta pulse recorded by the Tektronix TDS 210 oscilloscope. The reading shows a unipolar pulse suggesting effective charge collection after a beta particle interacts with diode B1.

Only one beta pulse test was able to be conducted however these exciting early results justify further testing on B1 as well as new testing opportunities for B2.

11.6 Device Structural Evaluation

Structure (a) was the initial experiment design and would theoretically provide the highest level of structural integrity, diamond surface contact, and lowest production cost. Unfortunately, the silicon base lead to fragility within the diamond membrane during the etches. Because of this, etching proved to be the major workflow constraint in the fabrication process as the diamond membrane became very brittle and frequently broke under low amounts of external pressure.

After many unsuccessful attempts to produce design (a), the remaining two structures were theorised and considered as alternatives that eliminated the silicon etching step. It was ultimately decided that design (b) would be the successor to the project as it had the combined benefit of no etching and no need for masking to get selective layer growth as seen in (c).

The reliability of the wiring method is also an important topic of discussion. Application of silver dag formed a fragile connection between the wire and metal contacts on the diodes. These connections were prone to breakage and had a significant impact on current-voltage characteristics. For this reason, the method of application of silver dag and wiring should be a fabrication process considered for optimisation.

All devices produced were polycrystalline diamond which have significant grain boundaries, especially compared to single crystal diamond which has no graining. At the time of writing, heteroepitaxial single crystal diamond growth (as shown by Schrek et al.) is not a feasible method of fabrication of the betavoltaic device[73]. Due to single crystal diamond's favourable electrical characteristics, it is a fair hypothesis to suggest such a device would exhibit lower leakage current and stronger forward current voltage[73].

Regardless of electrical results, each of the constructed diodes have structural points of improvement to be considered. For design (a) the fundamental roadblock to what could be a highly successful diode is the silicon etching process. If a suitable, repeatable etching process can be determined through use of current data and further testing, the device can certainly be scaled up to industry levels of production. In the case of design (b), this thesis proposes adapting the diode into a pseudo-vertical structure. While this slightly increases complexity in the initial growth phase, it would make the final step of wire application easier and more stable, thus better suited to product applications.

12. Conclusion

Spanning two device architectures and nine attempted prototype devices, one device with measurable diode characteristics was produced. Struggles with fabrication of a diamond membrane through a silicon base reduced the project scope, however the process is now better understood.

Multiple current-voltage tests conducted showed that device B2 displayed varying characteristics with weak PIM, MIM, and Zener diode appearances dependent upon operation conditions. The IV graphs were non-linear and generally displayed a strong reverse leakage current in the same order of magnitude as the forward voltage current. While this characteristic generally inhibits the diodes use in a nuclear micro battery due to decreased efficiency and lower power output, the device may still have alternative opportunities for use.

While device B1 did not show diode characteristics in the electrometer readings, further tests using the oscilloscope showed a successful unipolar beta pulse transmission. This is vital for the development of a nuclear micro battery; however further optimisations are necessary to generate useful magnitudes of performance.

13. Future Work

13.1 Fabrication improvements

In the interest of diode design (a), the clear next step is optimisation of the etching phase of production. While the unpredictability of silicon etch rates is a clear hindrance to etching success, it should not be seen as a complete inhibition of progress. Results from this report provide a foundation of knowledge for further work into the creation of a diamond membrane. Outside the bounds of time constraints, it is certainly possible to create a repeatable, efficient etching recipe that leads to production of a highly tuneable and more cost-effective diamond diode.

By perfecting the fabrication of diode (a), experimentation could be conducted on device performance as a result of varying dopant concentrations in the p-layer. By eliminating the need for a pre-grown surface (as seen in diode (b)), the device becomes more tuneable, and a more effective tool for comparison.

Rectification was shown to be optimizable purely through reapplication of the wiring, this allows for achievable and low-cost improvement, although the magnitude of enhancement is likely less significant than what could be possible through other adjustments. Changing the metal used for contact is a potential avenue for performance enhancement. Aluminium has been experimentally displayed to form a Schottky barrier on both oxygen and hydrogen terminated diamond semiconductor surfaces, therefore this may have limited device performance; swapping the ohmic contact for alternative metals such as gold could see major improvements.[55]

13.2 Further Characterisation

The University of Bristol is home to the NanoESCA facility, housing various state of the art surface characterisation and analysis techniques. This includes Photoemission Electron Microscope (PEEM) and high-resolution X-ray Photoelectron Spectroscopy (XPS). A Scanning Electron Microscope (SEM) Unit is also contained in the School of Chemistry. PEEM can characterise the diamond surface using electron emission to generate images over an area as small as 3 μm with a lateral resolution of 13 nm. This non-destructive characterisation technique would be valuable for visualising semiconductor surface variations. XPS would be useful for composition analysis of the diodes. By irradiating the diode with x-rays, electrons can be emitted with an energy proportional to the binding energy of the compound – this allows determination of the surface makeup in the top 1-10 nm of the sample. Because of this, XPS would be a useful tool determining dopant concentration and defect presence. SEM provides high magnification imaging, allowing for analysis of sample grain size and defect presence. These three characterisation techniques would all be useful going forward for performance comparison to see what conditions and device composition give the best diode characteristics.

13.3 Exploring Device Capabilities

Although the device did not display optimal PIM diode characteristics it is not rendered useless. The diode has the potential to operate as a sensor, seen by its responsiveness to 20 keV electrons in the e-beam, this suggests the diode could detect and provide feedback on radiative environments. An important factor for any device in the field of betavoltaics is lifespan; measuring device degradation after being subjected to controlled levels of beta radiation would provide a useful benchmark for device longevity.

13.4 Radioisotope implantation

Recent work, including that by my peer Axel Persson, has investigated the implantation of deuterium into the diamond lattice. The purpose of this is to determine if significant degradation occurs and if electrical characteristics such as Schottky barrier height are affected. Further work in this area could benefit the development of higher size and power efficiency betavoltaic devices. If implantation is successful with minimal impact on electrical characteristics, it paves the way for production of diodes in which the radioisotope is incorporated into the semiconductor bulk. This has the potential to be a safer, smaller and more efficient device.

14. References

1. B. W. Brook, A. Alonso, D. A. Meneley, J. Misak, T. Blees and J. B. van Erp, *Sustainable Materials and Technologies*, 2014, **1-2**, 8-16.
2. R. C. Ewing, R. A. Whittleston and B. W. D. Yardley, *Elements*, 2016, **12**, 233-237.
3. H. Zhu, Y. Deng, R. Zhu and X. He, *Regional Science and Urban Economics*, 2016, **60**, 139-154.
4. M. Greenberg and H. B. Truelove, *Risk Analysis*, 2011, **31**, 819-831.
5. Google Trends search data for "Diamond", "Carbon" and "Graphite", Google Trends, https://trends.google.com/trends/, (accessed 07/04, 2025).
6. A. Haghi, F. Naghiyev and S. Abdullayeva, *Advanced Computational Techniques in Nanoscience*, 2013, 1-103.
7. R. Nix, Miller Indices (hkl), https://chem.libretexts.org/@go/page/25363, (accessed 08/01, 2025).
8. ElementSix, CVD diamond handbook, https://e6cvd.com/media/wysiwyg/pdf/Diamond_Handbook_2024.pdf, (accessed 09/01, 2025).
9. Q. Su, Y. Xia, L. Wang, J. Liu and W. Shi, *Applied Surface Science*, 2006, **252**, 8239-8242.
10. G. Conte, M. C. Rossi, S. Salvatori, F. Tersigni, P. Ascarelli and E. Cappelli, *Applied Physics Letters*, 2003, **82**, 4459-4461.
11. C. J. H. Wort, C. S. J. Pickles, A. C. Beale, C. G. Sweeney, M. R. McClymont, R. J. Saunders, R. S. Sussmann and K. L. Lewis, 1999.
12. J. E. Field, *The properties of natural and synthetic diamond*, Academic Press, London u.a., 1992.
13. P. Nath and K. L. Chopra, *Thin Solid Films*, 1974, **20**, 53-62.
14. D. Halliday, R. Resnick and K. S. Krane, *Physics, Volume 2*, John Wiley & Sons, 2010.
15. J. Isberg, J. Hammersberg, E. Johansson, T. Wikström, D. J. Twitchen, A. J. Whitehead, S. E. Coe and G. A. Scarsbrook, *Science*, 2002, **297**, 1670-1672.
16. P.-N. Volpe, P. Muret, J. Pernot, F. Omnès, T. Teraji, F. Jomard, D. Planson, P. Brosselard, N. Dheilly, B. Vergne and S. Scharnholtz, *physica status solidi (a)*, 2010, **207**, 2088-2092.
17. M. S. Whittingham, *Chemical Reviews*, 2004, **104**, 4271-4302.
18. M. S. Whittingham, *Journal of The Electrochemical Society*, 1975, **122**, 526.
19. C. Curry, *Bloomberg New Energy Finance*, 2017, **5**, 43.
20. H. Qu, S. Wei and Z. Guo, *J. Mater. Chem. A*, 2013, **1**.
21. A. D. Pathak, S. Saha, V. K. Bharti, M. M. Gaikwad and C. S. Sharma, *Journal of Energy Storage*, 2023, **61**, 106792.
22. M. B. Naseem, H. S. Kim, J. Lee, C. H. Kim and S.-I. In, *The Journal of Physical Chemistry C*, 2023, **127**, 7565-7579.
23. P. Laurens, A. Piwnica, C. Reidemeister, W. M. Chardack and A. A. Gage, *Cardiac pacing. Assen: Van Gorcum & Comp*, 1973, 198-208.
24. M. R. Werner and W. R. Fahrner, *IEEE Transactions on Industrial Electronics*, 2001, **48**, 249-257.
25. J. E. Graebner, S. Jin, G. W. Kammlott, J. A. Herb and C. F. Gardinier, *Nature*, 1992, **359**, 401-403.

26. C. D. Clark, P. J. Dean, P. V. Harris and W. C. Price, *Proceedings of the Royal Society of London. Series A. Mathematical and Physical Sciences*, 1997, **277**, 312-329.
27. F. Zhao, Y. He, B. Huang, T. Zhang and H. Zhu, *Materials (Basel)*, 2024, **17**.
28. H. M. Strong, *American Journal of Physics*, 1989, **57**, 794-802.
29. S. S. Dossa, I. Ponomarev, B. N. Feigelson, M. Hainke, C. Kranert, J. Friedrich and J. J. Derby, *Journal of Crystal Growth*, 2023, **609**, 127150.
30. M. De Feudis, 2018.
31. J. M. T. Thompson and P. W. May, *Philosophical Transactions of the Royal Society of London. Series A: Mathematical, Physical and Engineering Sciences*, 2000, **358**, 473-495.
32. J.-h. Jiang and Y. Tzeng, *AIP Advances*, 2011, **1**, 042117.
33. N. Ohtake and M. Yoshikawa, *Journal of The Electrochemical Society*, 1990, **137**, 717.
34. M. Ashfold, P. May, J. Petherbridge, K. Rosser, J. Smith, Y. Mankelevich and N. Suetinb, *Physical Chemistry Chemical Physics - PHYS CHEM CHEM PHYS*, 2001, **3**, 3471-3485.
35. P. K. Bachmann, D. Leers and H. Lydtin, *Diamond and Related Materials*, 1991, **1**, 1-12.
36. L. G. Wang and A. Zunger, *Physical Review B*, 2002, **66**, 161202.
37. V. V. S. S. Srikanth, P. Sampath Kumar and V. B. Kumar, *International Journal of Electrochemistry*, 2012, **2012**, 218393.
38. R. Zulkharnay, G. Zulpukarova and P. W. May, *Applied Surface Science*, 2024, **658**, 159776.
39. G. Wan, M. Cattelan and N. A. Fox, *The Journal of Physical Chemistry C*, 2019, **123**, 4168-4177.
40. J. V. Macpherson, *Physical Chemistry Chemical Physics*, 2015, **17**, 2935-2949.
41. R. L. Boylestad, *Electronic Devices and Circuit Theory, 11e*, Pearson Education India.
42. M. I. Landstrass, M. A. Plano, M. A. Moreno, S. McWilliams, L. S. Pan, D. R. Kania and S. Han, *Diamond and Related Materials*, 1993, **2**, 1033-1037.
43. K. E. Bower, Y. A. Barbanel’, Y. Shreter and G. W. Bohnert, *Polymers, phosphors, and voltaics for radioisotope microbatteries*, 2002.
44. V. S. Bormashov, S. Y. Troschiev, S. A. Tarelkin, A. P. Volkov, D. V. Teteruk, A. V. Golovanov, M. S. Kuznetsov, N. V. Kornilov, S. A. Terentiev and V. D. Blank, *Diamond and Related Materials*, 2018, **84**, 41-47.
45. G. R. Mackenzie, S. Kaluvan, P. G. Martin, C. Hutson, T. Connolley, M. Cattelan, H. Dominguez-Andrade, T. L. Martin, N. A. Fox and T. B. Scott, *Materials Today Energy*, 2021, **21**, 100688.
46. F. Bouzid, E. Kayahan and F. Pezzimenti, *Applied Physics A*, 2023, **129**, 554.
47. B. R. Nullmeyer, J. W. Kwon, J. D. Robertson and A. Y. Garnov, *Sci Rep*, 2018, **8**, 12404.
48. S. Sze and K. K. Ng, *Physics of Semiconductor Devices: Third Edition*, 2006, 1-815.
49. T. Soga, in *Nanostructured Materials for Solar Energy Conversion*, ed. T. Soga, Elsevier, Amsterdam, 2006, pp. 3-43.
50. R. Zulkharnay and P. W. and May, *Functional Diamond*, 2024, **4**, 2410160.

51. V. S. Bormashov, S. A. Terentiev, S. G. Buga, S. A. Tarelkin, A. P. Volkov, D. V. Teteruk, N. V. Kornilov, M. S. Kuznetsov and V. D. Blank, *Diamond and Related Materials*, 2017, **75**, 78-84.
52. B. L. Smith and E. H. Rhoderick, *Solid-State Electronics*, 1971, **14**, 71-75.
53. C. Delfaure, M. Pomorski, J. de Sanoit, P. Bergonzo and S. Saada, *Applied Physics Letters*, 2016, **108**, 252105.
54. J. Cañas and D. Eon, *Diamond and Related Materials*, 2023, **136**, 110038.
55. K. Tsugawa, H. Noda, K. Hirose and H. Kawarada, *Physical Review B*, 2010, **81**, 045303.
56. S. Koné, G. Civrac, H. Schneider, K. Isoird, R. Issaoui, J. Achard and A. Gicquel, *Diamond and Related Materials*, 2010, **19**, 792-795.
57. W. Mönch, *Europhysics Letters*, 1994, **27**, 479.
58. W. Ji, J.-B. Kim and J.-J. Kim, *Nuclear Engineering and Technology*, 2022, **54**, 3811-3815.
59. M. A. Prelas, C. L. Weaver, M. L. Watermann, E. D. Lukosi, R. J. Schott and D. A. Wisniewski, *Progress in Nuclear Energy*, 2014, **75**, 117-148.
60. G. Chicot, D. Eon and N. Rouger, *Diamond and Related Materials*, 2016, **69**, 68-73.
61. D. Zhao, C. Hu, Z. Liu, H.-X. Wang, W. Wang and J. Zhang, *Diamond and Related Materials*, 2017, **73**, 15-18.
62. P. Rappaport, *Physical Review*, 1954, **93**, 246-247.
63. F. Bouzid, F. Pezzimenti and L. Dehimi, *Nuclear Instruments and Methods in Physics Research Section A: Accelerators, Spectrometers, Detectors and Associated Equipment*, 2020, **969**, 164103.
64. T. Shimaoka, H. Umezawa, K. Ichikawa, J. Pernot and S. Koizumi, *Applied Physics Letters*, 2020, **117**, 103902.
65. B. J. Baliga, *IEEE Electron Device Letters*, 1989, **10**, 455-457.
66. B. Kindler, A. Beusch, W. Hartmann, A. Hübner, B. Lommel, J. Steiner and V. Yakusheva, *Journal of Radioanalytical and Nuclear Chemistry*, 2014, **299**, 1141-1143.
67. M. Severini, Keithley 2401 SMU Source Meter Unit, https://www.sglabs.it/en/product.php?s=keithley-2401&id=2245, (accessed 05/04, 2025).
68. I. Tsemenko, Keithley 6517A electrometer restoration project, https://xdevs.com/fix/k6517a_u2/, (accessed 05/04, 2025).
69. D. Altobelli and D. Taylor, Electron gun (BEAM) systems: Kimball Physics: Electron and Ion Gun Systems, https://www.kimballphysics.com/learning_center/electron-gun-beam-systems/, (accessed 07/04, 2025).
70. V. A. Sidorov and E. A. Ekimov, *Diamond and Related Materials*, 2010, **19**, 351-357.
71. V. Mortet, Z. Vlčková Živcová, A. Taylor, O. Frank, P. Hubík, D. Trémouilles, F. Jomard, J. Barjon and L. Kavan, *Carbon*, 2017, **115**, 279-284.
72. S. Tan, R. A. Boudreau and M. L. Reed, *Sensors and Materials*, 2001, **13**, 303-313.
73. M. Schreck, S. Gsell, R. Brescia and M. Fischer, *Scientific Reports*, 2017, **7**, 44462.

15. Appendix

15.1 The diamond membrane – A comprehensive review

As discussed in this report, a key factor that limited lead times and diode development was the manufacturing of a successful diamond membrane in the reverse of the silicon chip used for epitaxy. The entire process involved laser ablation to remove the majority silicon substrate before a more delicate KOH wet etching procedure.

The most successful sample etching process was A3 which successfully produced a diamond membrane however the membrane ended up fracturing during cleaning. For this reason, the process for A3 is described in the most detail however other conditions are also noted.

15.1.1 Laser Ablation A3

Height profile analysis produced using the LEXT microscope show the change in etch depth after every laser and KOH etch during the production of sample A3. This provides the most comprehensive report of the etching process from start to finish.

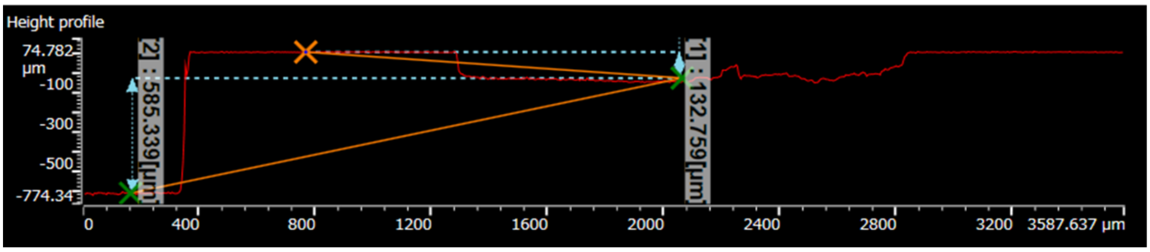

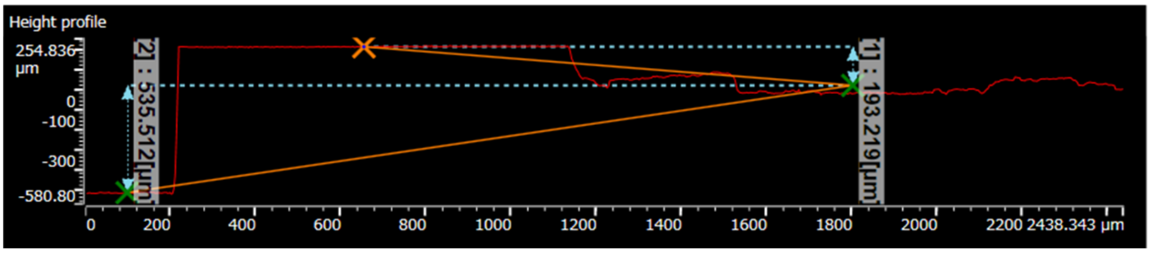

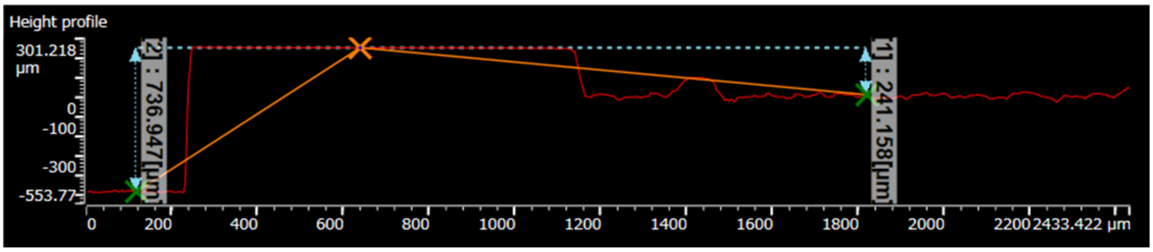

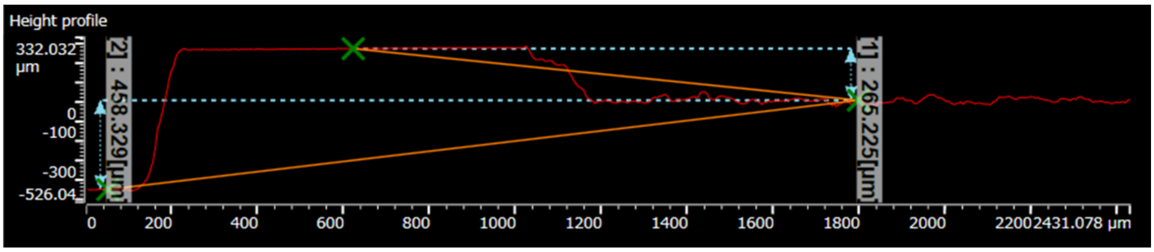

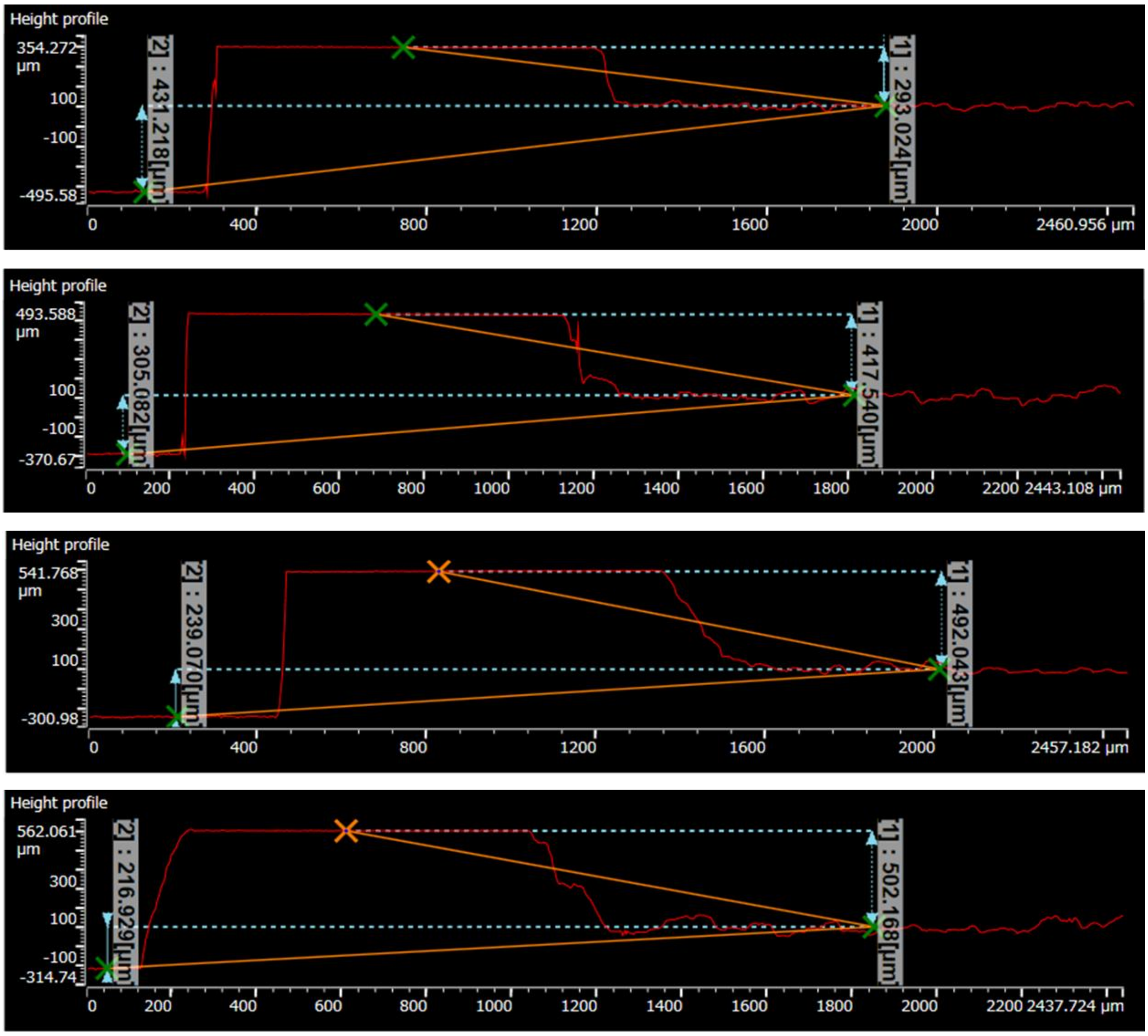

Figure 34 - A collation of the eight laser ablation height profile analyses for sample A3.

Figure 34 shows in detail the change in etch depth after each laser etching sequence. The specific conditions for each pass can be seen below:

Table 7 - The etching conditions and total etch height for each pass in the laser ablation of sample A3

Etch Number	**Etch Power / %**	**Number of Passes**	**Etch Speed/ mm/s**	**Total Etch Height / µm**
1	30	6	4	135.76
2	30	4	3	193.22
3	30	8	3	241.16
4	40	4	3	265.23
5	40	7	3	293.02
6	40	4	3	417.54
7	40	6	4	492.04
8	45	4	3	502.17

This was the most successful laser ablation sequence and showed steady etch depth increases. The lower power and number of passes per etch could potentially have aided the process due to a lower build up of grainy white solid (thought to be SiO_2 produced via etching).

15.1.2 KOH Etching A3

Aside from the application of a Kapton mask, the KOH etching procedure was relatively straightforward. The masked sample was attached to a fishhook-style wire and suspended in 75 ml of KOH at the desired concentration and temperature.

Application of the mask was slightly trickier and the method that minimised risk of damage to the device involved pre-cutting a small hole (approximately 1 x 1 mm) in the Kapton tape before sealing the device inside with the hole positioned accordingly over the recess.

Height profile reports for the KOH etching process can be seen below:

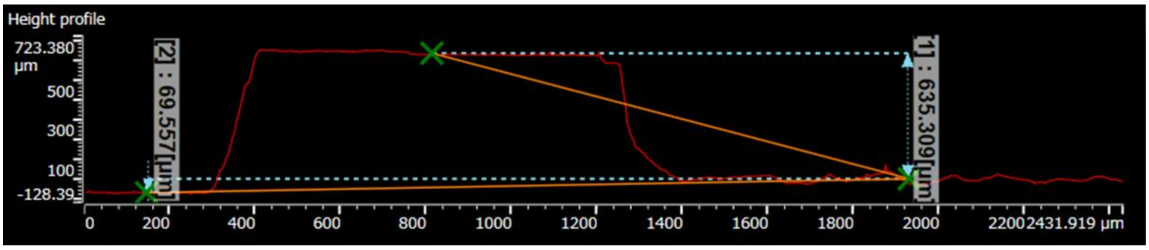

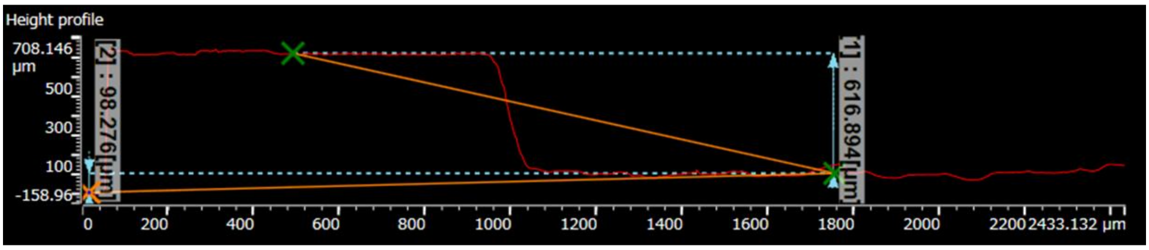

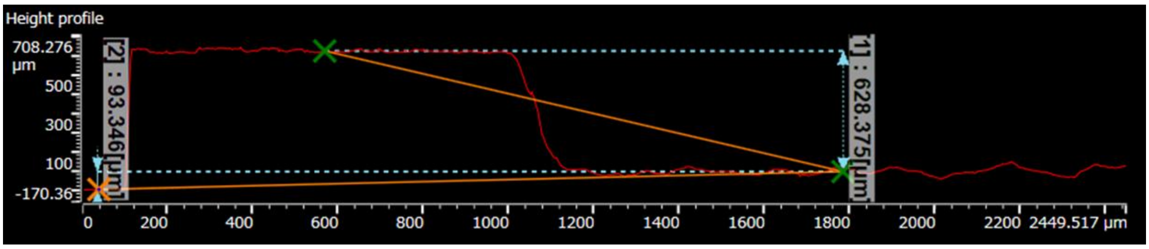

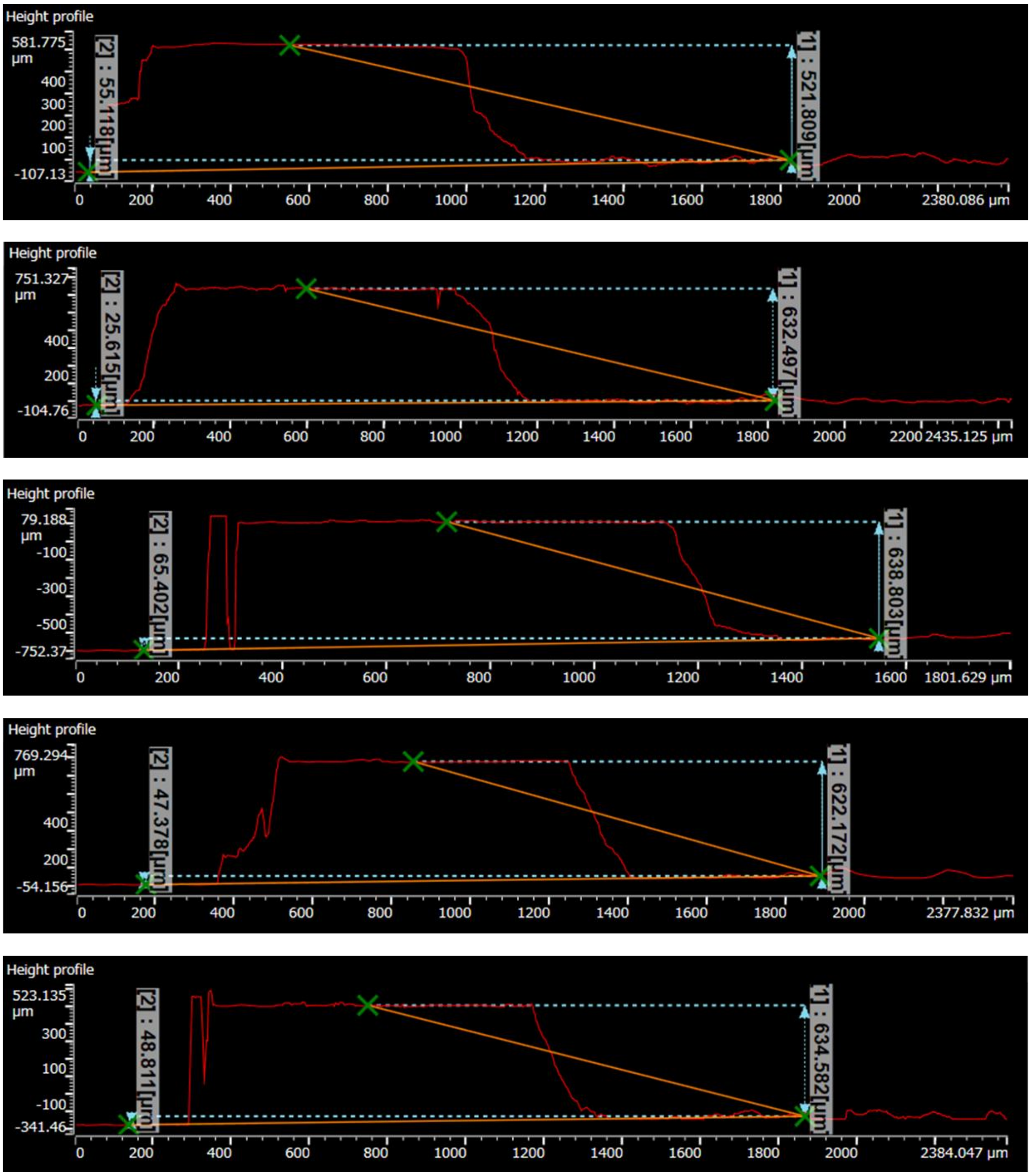

Figure 35 - A collation of the eight KOH etches height profile analyses for sample A3.

Table 8 - A complete list of etch heights during the KOH etching sequence of sample A3. Every etch was carried out in 5 M KOH at 80 °C for 60 minutes. Inconsistencies in the approximate etch height are highlighted in red. The approximate etch height is calculated by adding the difference in the measured height to the initially calculated total height at the start of laser etching, this accounts for loss of silicon height through Kapton tape degradation.

Etch Number	**Etch Depth / µm**	**Height to base / µm**	**Approx Total etch height / µm**
1	635.31	69.56	650
2	616.89	98.28	621
3	628.38	93.35	626
4	521.81	55.12	665
5	632.50	25.62	694
6	638.80	65.40	655
7	622.17	47.38	672
8	634.58	48.81	671

Large variations in the etch height measurements are thought to be caused by two key factors, debris build up in the recess and poor calibration of the LEXT microscope. Debris may produce smaller etch height measurements while poor calibration can lead to under or overestimates in etch depth.

15.2 Further Sample Etching Results

While the data from sample A3 appears to provide the best reference point for future etching attempts, further sample data is included for completeness.

15.2.1 Sample A4

To try and reduce production times, higher power and passes per etch were trialled on sample A4.

Table 9 - The shorter etching process for sample A4. The increased power and number of passes reduced processing time for the sample and produced a good diamond membrane which ultimately ended up breaking in a subsequent, KOH etching step.

Etching Step	**Etch power / %**	**Number of Passes**	**Etch Speed / mm/s**
Laser 1	40	8	3
Laser 2	50	8	3
Laser 3	40	8	3

After three successful laser etches were completed, sample A4 was subjected to the standard wet etching procedure with 7 M KOH at 90 °C. On the fourth submersion, a small hole was made in the membrane meaning it could no longer be used. This was however, a slightly better result than sample A3 in which the entire membrane broke. Although only a small hole formed in the membrane, the lower power, longer etching process of sample A3 is still favoured. This is because the process is more adjustable over a longer period of time and has a larger margin for error with more opportunity to end etching early and analyse the membrane.

15.2.2 Sample A5

After some progress in understanding the laser etching process from the previous sample, slightly higher power etches were trialled again however inconsistent etch rates proved to be another source of hindrance.

Table 10 - The etching sequence for sample A5, another promising sequence which ended prematurely after the entire membrane disconnected from the chip when submerged on the fourth wet etch.

Etching Step	Etch power / %	Number of Passes	Etch Speed / mm/s	Time in solution / minutes	Solution Temperature / °C
Laser 1	40	8	3	-	-
Laser 2	50	8	3	-	-
Laser 3	40	8	3	-	-
7 M KOH 1	-	-	-	60	90
Laser 4	45	10	3	-	-
Laser 5	50	8	3	-	-
7 M KOH 2	-	-	-	60	90
7 M KOH 3	-	-	-	60	90
Laser 6	60	1	3	-	-
Laser 7	70	3	3	-	-
7 M KOH 4	Membrane broke after submersion.				

The etching sequence for sample A5 highlighted a key issue with the inconsistency of the etching process. As you can see the sequence operated at a higher laser power, with more passes than for A4. In addition, the wet etching process was conducted at higher temperatures and molarities. Despite this, the procedure contained far more steps than that for sample A4.